Quantitative Susceptibility Mapping in Ischemic Stroke: Cerebral Veins, Tissue, and Microbleeds

by

Parisa Badihi Najafabadi

A thesis submitted in partial fulfillment of the requirements for the degree of

Master of Science

Department of Biomedical Engineering
University of Alberta

Abstract

Quantitative susceptibility mapping (QSM) is an emerging magnetic resonance imaging (MRI) post-processing technique that uses phase images from a gradient echo sequence to create magnetic susceptibility maps. QSM is sensitive to paramagnetic iron found in various states of blood, from deoxyhemoglobin to hemosiderin. QSM can also differentiate between calcium and iron deposits. Unlike phase images, QSM is not strongly dependent on object shape nor orientation with respect to the main magnetic field. A 3D flow-compensated gradient echo was used in this work for reconstruction of QSM from phase images. An introduction to MRI, phase images, susceptibility and susceptibility-weighted imaging (SWI) is given in Chapter 1. This chapter will also explain the details of QSM reconstruction and an overview to various applications.

Tissue and draining vein oxygenation level in the brain is a prominent parameter in determining the severity of ischemia. Due to its sensitivity to deoxyhemoglobin, QSM provides a quantitative measure of brain tissue and venous oxygenation. QSM can also distinguish between cerebral microbleeds (CMBs) and calcium deposits and provides valuable information of the size and quantity of CMBs. Chapter 2 introduces stroke, with a focus on ischemic stroke and cerebral microbleeds, as the major clinical applications of this research.

Recent studies in ischemic stroke using QSM have only examined severe ischemic strokes. Furthermore, no studies to date have examined all three

potential applications of QSM to ischemic stroke: cerebral microbleed quantification, and vein and tissue oxygenation. In Chapter 3, the value of QSM in ischemic stroke patients was investigated in two ways. First, by evaluating susceptibility in tissue and draining veins from infarcted and contralateral regions in acute stroke with a wide range of stroke severity; and second, assessing microbleed burden on QSM in comparison to standard SWI in chronic stroke.

QSM analysis in acute ischemic stroke revealed significantly greater susceptibility ($p< 0.001$) for vein measurements in the infarcted hemisphere compared to the contralateral homologous hemisphere. This can be an indicator of higher blood deoxygenation in veins draining from the infarcted hemisphere, suggesting a compromised arterial blood flow and collateral vascular distribution in the ischemic region. Tissue analysis showed a significantly higher susceptibility ($p< 0.036$) of white matter in infarcted regions compared to healthy regions which can be an indicator of higher deoxygenation in the infarct, while no significant higher susceptibility was observed in grey matter between the two hemispheres. This may be due to higher sensitivity of white matter to ischemia.

Microbleed assessment using QSM revealed key advantages of QSM over SWI, such as smaller size of microbleed ($p< 0.0001$) as well as potentially improved detectability of microbleeds. This provides quantitative measurement of susceptibility rather than the qualitative nature of SWI and removal of blooming signal artifacts originating from strong dipole field effects seen on SWI.

In summary, this thesis has demonstrated the value of QSM in ischemic stroke for measuring both oxygenation and microbleeds. Since QSM can be obtained from raw phase images of standard SWI sequences, no extra scan time is needed to enable QSM studies when SWI is already performed.

Preface

This thesis is an original work by Parisa Badihi Najafabadi. The research project makes use of in-vivo MRI data from two studies for which ethics approvals were granted by “University of Alberta Ethics Board, Project name: "Dabigatran Following Transient Ischemic Attack and Minor Stroke (DATAS) II", Pro00047362, 2014-2018” and “University of Alberta Research Ethics Board, Project name: "INSPIRE" Description: International Stroke Perfusion Imaging Registry, Pro00031331, 2013-Ongoing”.

To Maman, Baba and my amazing siblings Nahid and Mohammad

Contents

List of Tables

List of Figures

1. Introduction

1.1. Overview of Magnetic Resonance Imaging (MRI)

Magnetic resonance imaging (MRI) is a versatile imaging modality that is widely used clinically and can create functional and anatomical images of the human body. Numerous books and articles have described this technique very thoroughly (1-3) and here, only a brief description is provided as an introduction to this topic. For human MRI, the source of signal is usually hydrogen protons of water or fat. These hydrogen nuclei have a magnetic moment which arises from the nuclear spin. After the body is placed inside the magnet bore, the magnetic moments align in-direction or opposite to the main magnetic field B_0 (z-direction), forming a Boltzmann distribution. The transverse (x and y) components precess around z-axis at a fixed frequency known as the Larmor frequency, but since each spin has different phases, the net sum of transverse magnetization is zero. By applying a radio frequency (RF) wave at the Larmor frequency, spins can be torqued into the transverse plane and once the RF pulse is turned off, start precessing in the transverse plane. An electromotive force (emf) is induced in the RF receiver coils by spins' varying magnetic flux in the transverse plane. By using quadrature detection, two streams of signal with 90° phase difference would be received that make the complex signal with real and imaginary parts. Over time, the signal decays and returns to equilibrium.

To pinpoint the origin of the signal, three magnetic field gradients in each X, Y and Z directions are utilized to create small variations in the main magnetic field and hence, in the precession of protons. The gradients are used for slice, phase and frequency encoding. The resulting matrix of data with varying encodings is converted to MR images using the Fourier Transform.

The primary contrast mechanisms of MR images can be due to variable water concentration in different tissue (proton density), or relaxation weighting of recovery time or decay time. After the magnetization is torqued into the transverse plane, the x-y components of the magnetization start to dephase with time constant T_2, due to spin-spin interactions

(transverse relaxation). Also, the longitudinal magnetization starts to recover back to equilibrium along the z-direction with a time constant T_1, called longitudinal relaxation. Considering the time between each RF pulse to be the repetition time (TR), magnetization at echo time TE in a spin echo experiment can be calculated as:

$$M_{transverse} = M_0 \left(1 - e^{-TR/T_1}\right) e^{-TE/T_2} \quad (1.1)$$

with M_0 being the longitudinal equilibrium magnetization. In cases of no RF refocusing, magnetization experiences additional suppression due to external field inhomogeneities and T_2 would be replaced by a shorter relaxation time T_2*.

1.2. Magnitude and Phase Components of MRI

After the RF pulse is applied, the net precessing transverse magnetization creates the measurable signal. For standard gradient recalled echo (GRE) sequences (assuming 90° excitation pulse and long TR for full recovery) the decay of x-y components occurs with the time of T_2*, and at echo time TE the magnitude would be:

$$\left|M_{xy}\right| = M_0 . e^{-\frac{TE}{T_2^*}} \quad (1.2)$$

The phase of the signal is also changing with time and frequency. In general, phase varies with time and main magnetic field (Equation 1.3). In spin echo sequences, RF refocusing pulses ensure that phase effects are largely rewound. However, in gradient echo sequences, phase continues to evolve with time. While the gradients are reversed and balanced in a gradient echo sequence, there are additional magnetic fields besides B_0 and gradients such as chemical shift, susceptibility, imperfect shimming or eddy currents, that could cause changes in the precessing frequency as a result of field perturbations. This thesis is focused on susceptibility effects. As the time evolves, these phase shifts accumulate and can be defined as:

$$\varphi = -\gamma B_0 t \quad (1.3)$$

$$\Delta\varphi = -\gamma . \Delta B . TE \quad (1.4)$$

Phase images (Figure 1) can be obtained from MR real and imaginary components after Fourier Transform by:

$$\varphi = \tan^{-1}\frac{Imaginary}{Real} \quad (1.5)$$

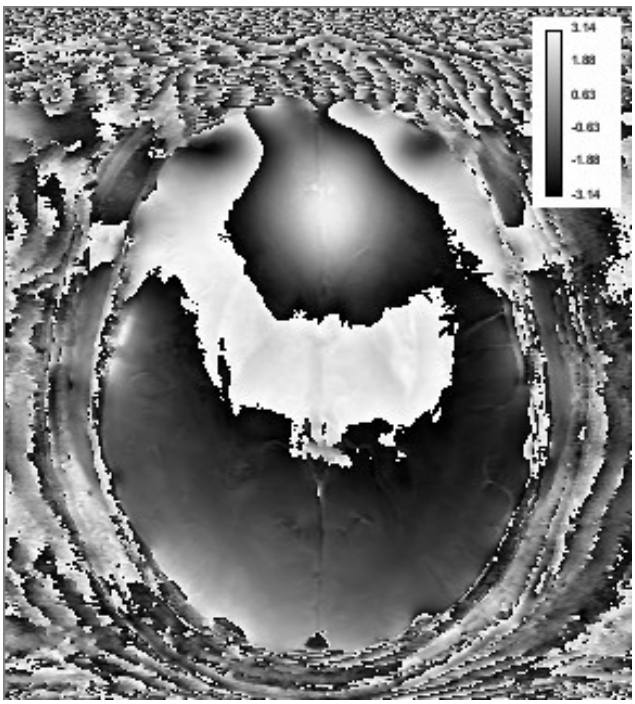

Figure 1 Phase image of a slice of brain from SWI sequence. Parameters: TE/ TR=20ms/ 28ms, Flip Angle=15, B_0=3 Tesla. Scale is in radians. Note the phase wrapping.

Studies show that in addition to the sources of phase in GRE images such as magnetic susceptibility, the phase is also dependent on the tissue architecture and how some magnetic susceptibility inclusions like deoxyhemoglobin, lipids, protein and none-heme iron are spatially distributed (4). This can help to delineate structures like putamen, globus pallidus and head of the caudate nucleus that are not clearly discriminated on T_1-weighted images (4).

In brain, phase imaging (5) delivers higher contrast-to-noise ratio compared to T_1 weighted imaging revealing substantial contrast between cortical grey and white matter (6). Phase images are also used for encoding flow (7), an area of imaging not considered here. When phase images are processed with magnitude images it is possible to create susceptibility-weighted images (SWI) explained in detail in section 1.3.2. Although phase

images have limitations such as the non-locality of the phase dipole signal and their dependency on the object shape and its orientation with respect to the field (4, 8), they have benefits over magnitude images for not being directly dependent on T_1 and T_2 relaxation parameters and being less affected by the increased inhomogeneity of radiofrequency magnetic fields at high main magnetic field strengths (9). These features make phase images a good candidate for quantitative measurements of tissue properties and their limitations can be addressed by using quantitative susceptibility mapping (QSM). Further details regarding processing of phase images and creating quantitative susceptibility maps are provided in section 1.4.

1.3. Susceptibility and Susceptibility Weighted Imaging (SWI)

1.3.1. Magnetic Susceptibility

Magnetic Susceptibility, denoted by χ, is an intrinsic tissue property that measures the ability of a material to be magnetized when placed in an external magnetic field (10), and unlike phase, is not dependent on time, magnetic field, orientation or shape. Therefore, susceptibility imaging would be able to reflect properties of tissue more consistently (9). Substances with magnetic susceptibility can develop a magnetic polarization when put inside a magnetic field. Most materials are classified into three groups of diamagnetic ($-1 < \chi < 0$) or say in the order of 10^{-6}, paramagnetic ($0 < \chi < 0.01$) or say in the order of 10^{-5} to 10^{-3}, or ferromagnetic ($\chi > 0.01$). For a diamagnetic substance an internal magnetic field is created in it after being put into the magnetic field that opposes the external field and overall, reduces its effect while for the other types the effect is augmenting the external magnetic field. Figure 2 illustrates the susceptibility spectrum and the relative place of biological tissue in this spectrum compared to other sources of susceptibility. It can be seen that biological tissue is in diamagnetic or weakly paramagnetic range (11).

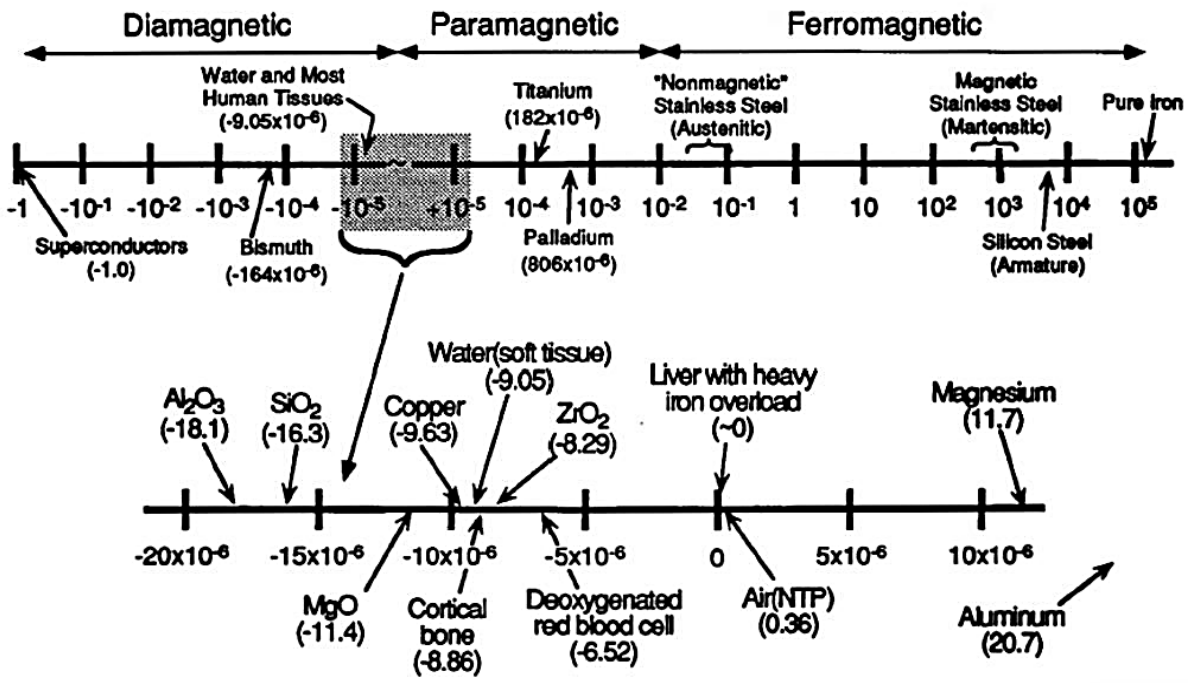

Figure 2 Susceptibility spectrum indicating water and most human tissue are in the range of diamagnetic to weakly paramagnetic (Formica and Silvestri,2004).

Susceptibility differences between two areas e.g. air-tissue interface, can cause a gradient in magnetic field that results in signal attenuation or distortions in images known as susceptibility artifact. Susceptibility artifacts can also have other sources such as metallic objects with high susceptibility that change the homogeneity of the magnetic field. Figure 3 shows an example of this negative effect of susceptibility in regions near air-tissue interface.

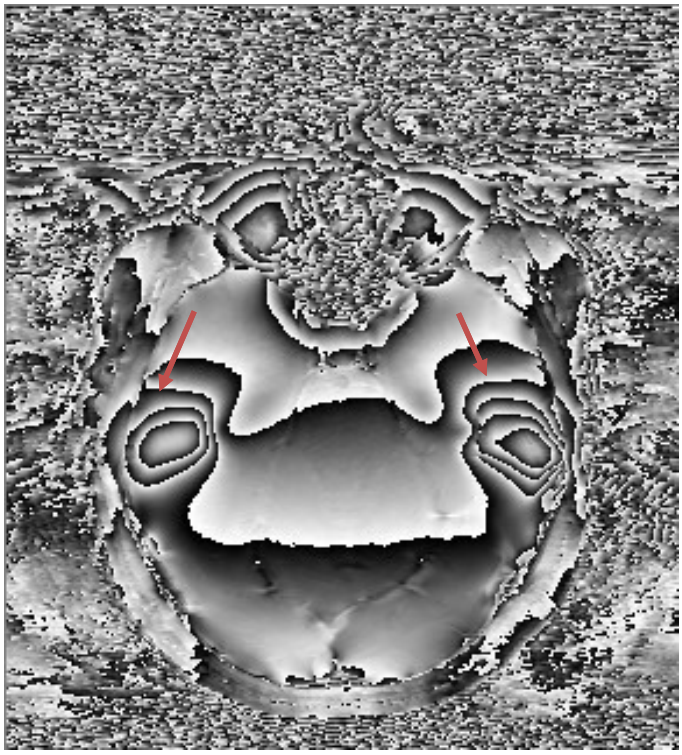

Figure 3 Phase image with susceptibility artifact in regions near air-tissue interface. The red arrows indicate areas near the ear canals, while the top of the image is near the frontal sinuses. Parameters: TE/ TR=20ms/ 28ms, Flip Angle=15°, B_0=3 Tesla.

However, contributions of susceptibility in phase can be used to improve magnitude contrast and is known as the SWI method that will be discussed in section 1.3.2. In addition, phase alterations due to susceptibility can be employed to find the local field shifts caused by the magnetic source and susceptibility distribution can be obtained by inverting the local field shift. Details for this method, known as quantitative susceptibility mapping, are expanded in section 1.4.

1.3.2. Susceptibility-Weighted Imaging

Susceptibility-weighted imaging is a 3D flow compensated technique that combines phase and magnitude GRE images to create an image by taking advantage of phase signal differences to enhance the T_2*-weighted magnitude contrast. Image contrast on SWI may arise from signal loss on magnitude images due to dephasing of the spins in the voxel or from

the phase images due to substances with different magnetic susceptibility than their surrounding tissue (10, 12). Figure 4 shows the pulse sequence used for SWI.

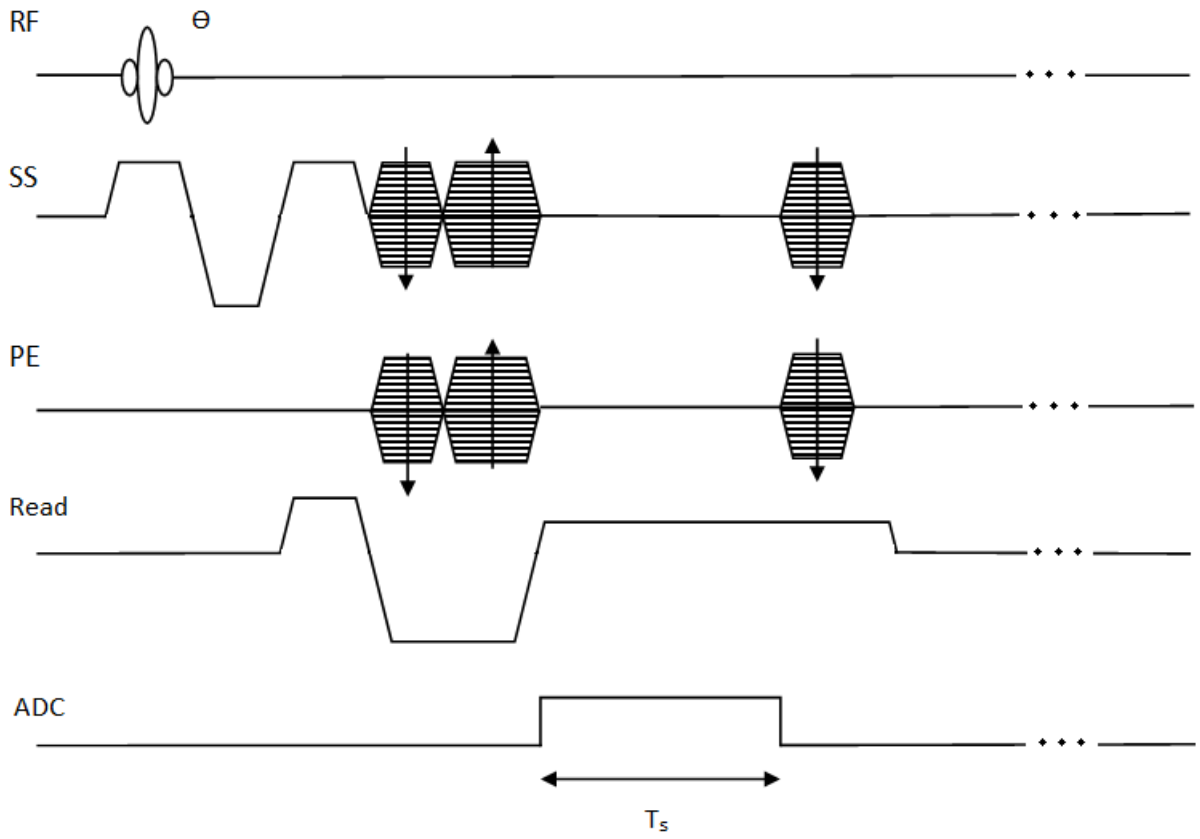

Figure 4 GRE sequence with gradient moment nulling of the first order of flow to achieve flow compensation. T_s, SS and PE are sampling time, slice selection gradient and phase encode, respectively.

The first step to create the SW images is to generate filtered-phase images that reflect susceptibility changes. This is feasible by applying a high-pass filter to phase images that removes the low-spatial frequency components (13). Although the created filtered phase shows the susceptibility contrast, it is affected by both internal and external field shifts within and outside of the susceptibility source which can impact the differentiation between neighboring tissue with different susceptibilities (13); thus, a mask created from filtered phase images is employed to improve the contrast of magnitude images. The phase mask has values between zero and one and is designed to set to unity when no change in magnitude is desired and to set to other numbers to decrease the signal intensity where phase takes certain values. For example, if the phase is negative, the mask for location *x* is defined as below:

$$f(x) = \begin{cases} (\pi + \varphi(x))/\pi, & -\pi < \varphi < 0 \\ 1, & otherwise \end{cases} \quad (1.6)$$

Equation 1.6 displays an equation that highlights the negative differences in phase, if the phase equals -π, signal will be suppressed, and for other values of phase between -π and zero, it will deliver a number between 0 and unity. This phase mask can be multiplied in magnitude images a number of times and change magnitude intensity based on the phase. Figure 5A and 5B show the phase profile with grey matter (GM), white matter (WM), cerebrospinal fluid (CSF) and vein components and the calculated mask for each one.

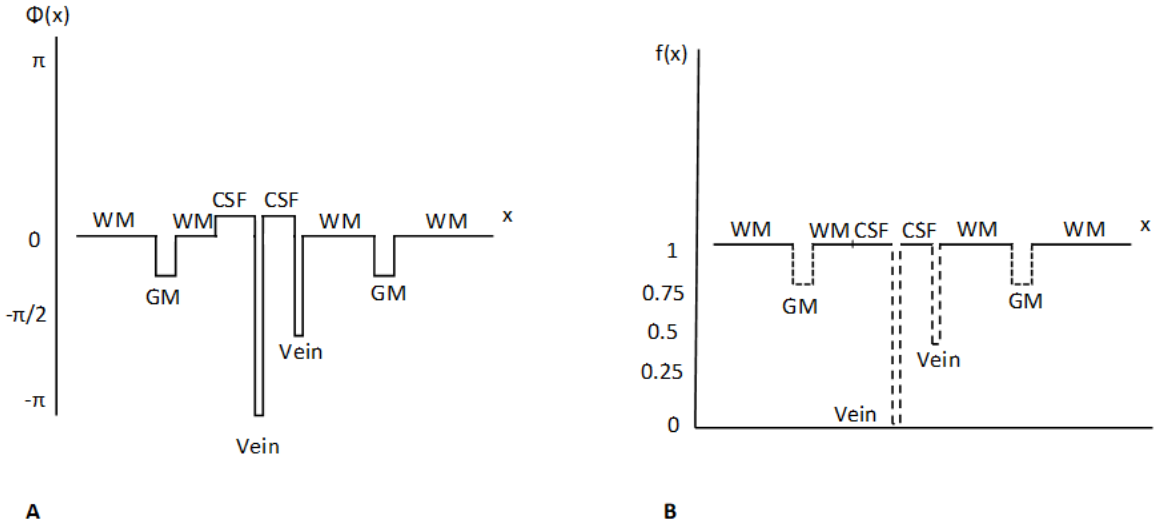

Figure 5 Phase profile containing grey matter, white matter, cerebrospinal fluid and veins (A), Phase mask (B)

1.3.3. SWI Applications

As it can be observed in figure 5B, magnitude images when multiplied by the phase mask would create a better differentiation between grey and white matter. Also, Figure 5B shows that veins are the components that get suppressed the most owing to deoxygenated blood with paramagnetic properties in the veins. This feature makes SWI a powerful tool to depict veins and other neurodegenerative and neurovascular diseases that have high amounts of deoxygenated blood or other paramagnetic sources like iron (14, 15). Examples of

pathological conditions such as hemorrhage, cerebral microbleeds and projection image of SWI to show vein continuity along the slices is shown in Figure 6.

1.4. Quantitative Susceptibility Mapping

Quantitative susceptibility mapping is a new technique to obtain quantified magnetic susceptibility maps by reconstructing the raw GRE phase images (9, 16, 17). Phase images have a non-local nature and phase signal can be affected in areas beyond the size of susceptibility source that perturbs the field and causes the variation in phase (18). Also, phase is dependent on the main magnetic field strength, echo time in GRE images and the geometry of involved structures and their relative orientation with respect to the main magnetic field. These complications can be overcome by creating susceptibility maps that reflect the intrinsic tissue magnetic property and composition (9).

In sections below the basic theory of QSM and the complete processing of QSM are explained in detail.

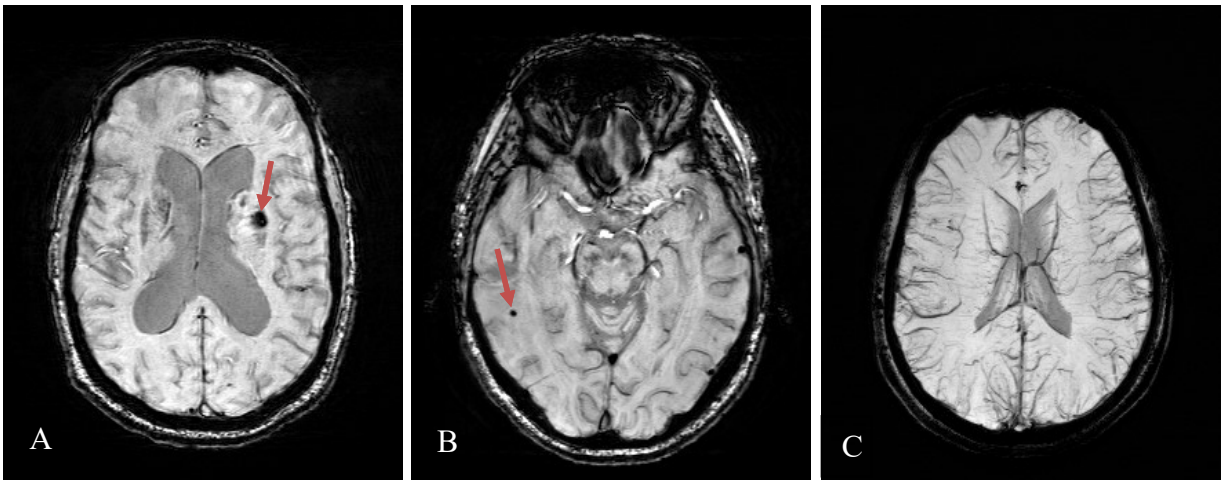

Figure 6 Examples of pathological conditions and vein demonstration on SW images. Cerebral hemorrhage (A). Cerebral microbleed (B). minimum intensity projection of SW images to show veins(C).

1.4.1. Theory

Recent theoretical developments have derived the equations that relate the phase changes to magnetic susceptibility distribution that originated the field perturbations (19-21). For gradient echo imaging, assuming that the main magnetic field B_0 is in z direction, with $\Delta Bz(\vec{r})$ being the z component of induced field perturbations, the phase in the image domain would be:

$$\varphi(\vec{r}) = \varphi_0(\vec{r}) + \gamma.\Delta Bz(\vec{r}).TE \quad (1.7)$$

Where $\varphi_0(\vec{r})$ is the coil-sensitivity dependent phase offset.

For $\chi \ll 1$, $\Delta Bz(\vec{r})$ can be related to susceptibility:

$$\Delta Bz(\vec{r}) = B0\,\chi(\vec{r}) * G(\vec{r}) \quad (1.8)$$

This gives the relative induced field perturbation $\frac{\Delta Bz(\vec{r})}{B_0}$, as a convolution of susceptibility distribution $\chi(\vec{r})$ and $G(\vec{r})$ the unit dipole response (called green's function), given by:

$$G(\vec{r}) = \frac{1}{4\pi}\frac{(3\cos^2\theta-1)}{r^3} \quad (1.9)$$

And θ is the angle between $\vec{r}$ and $\vec{z}$. The Fourier Transform of G ($\vec{r}$) is given by:

$$G(\vec{k}) = \begin{cases} \frac{1}{3} - \frac{k_z^2}{k^2}, & k \neq 0 \\ 0, & k = 0 \end{cases} \quad (1.10)$$

Therefore, by knowing the phase changes, local field shifts can be calculated and by using the equation below the susceptibility distribution can be obtained:

$$\chi(\vec{k}) = \frac{1}{G(\vec{k})}\frac{\Delta Bz(\vec{k})}{B_0} \quad (1.11)$$

The process of calculating $\chi(\vec{k})$ from $\frac{\Delta Bz(\vec{k})}{B_0}$ is called dipole inversion or susceptibility inversion. However, the inversion process becomes ill-posed due to zero cones where $G(\vec{k})$

equals zero. Figure 7 shows the zero cones in $G(\vec{k})$ at the magic angle (22). The susceptibility inversion algorithms try to properly calculate the susceptibility, details regarding this topic are discussed in section 1.4.5.

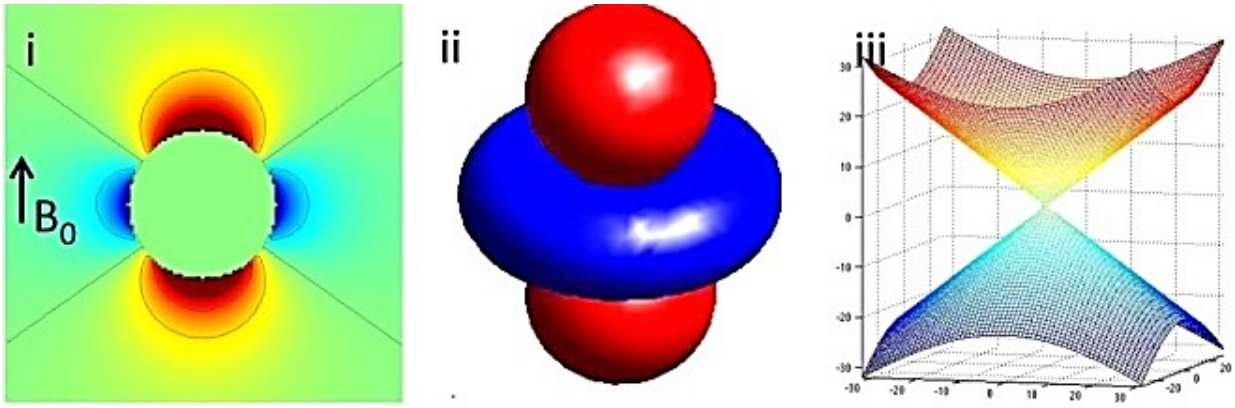

Figure 7 The ill-posed problem of the dipole inverse. (i) Sagittal section of the unit dipole field (ii) and its surface contour. (iii) The zero cone surfaces of the dipole kernel in k-space. (from Wang Y and Liu T. MRM. 2015)

The QSM pipeline is illustrated in Figure 8.

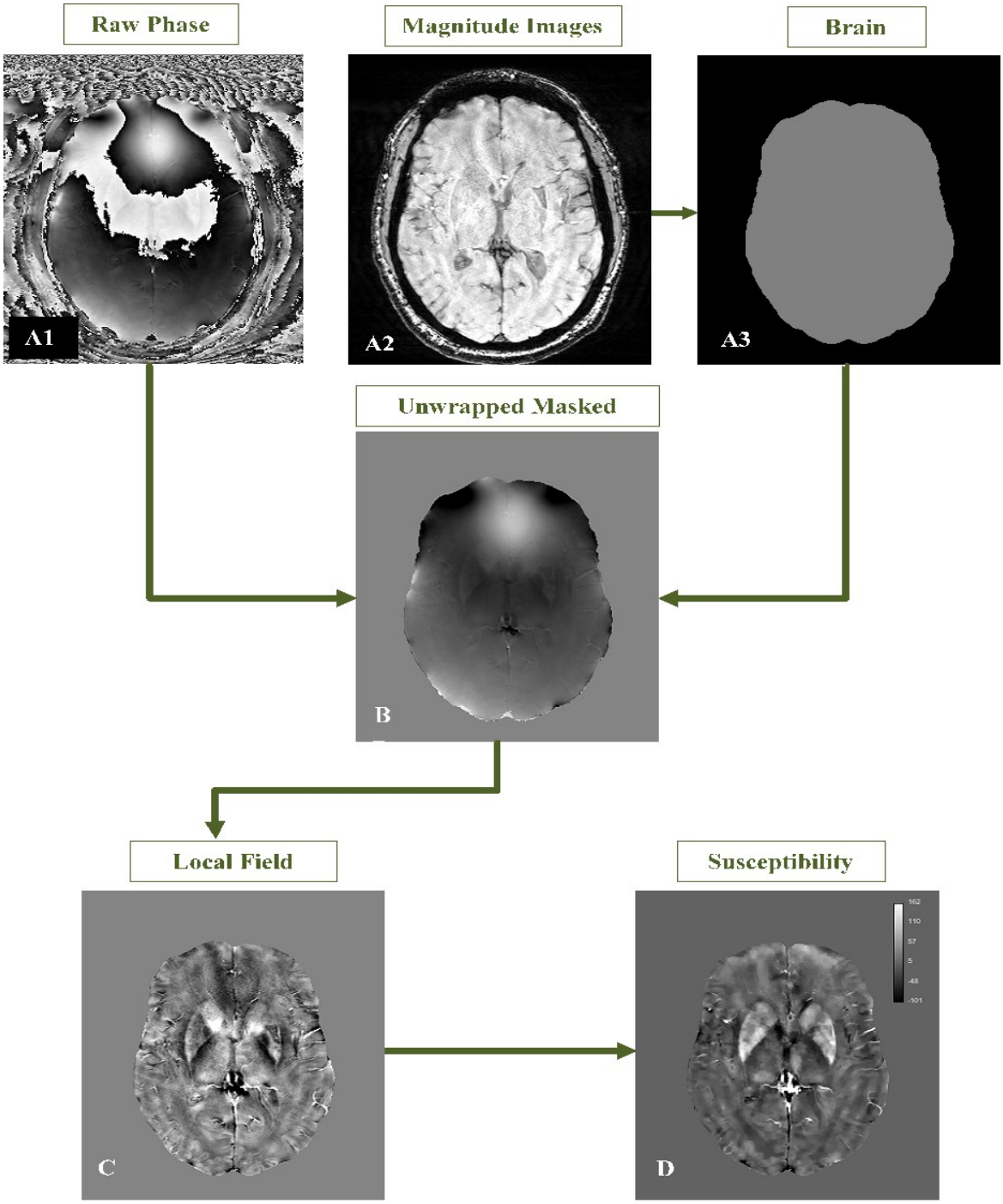

Figure 8 Schematics for quantitative susceptibility mapping. Raw phase from gradient echo sequence is multiplied in a mask using magnitude image to extract brain (A1-3). Phase is unwrapped (PRELUDE)(B). Background field removed (RESHARP) to separate background phase from phase contributed by the brain tissue (C). calculating magnetic susceptibility from local field shift (in ppb) (D).

1.4.2. Phase Unwrapping

As mentioned in previous sections, phase images are used to calculate the magnetic susceptibility distribution from the phase that has accumulated with time from field perturbation. MRI data is collected as complex vectors and phase, as the angle of the vector can have values between [-π, π). When the phase value exceeds this limit, phase becomes aliased and gets wrapped. Phase unwrapping is seen as phase discontinuities in the images. In the situation of phase wrapping, the actual phase which follows the equation (1.12) can be recovered and unaliased using the process known as phase-unwrapping.

$$\varphi_{actual} = \varphi_{measured} + n.2\pi \quad (1.12)$$

Figure 9 shows an example of phase image before and after execution of a phase unwrapping algorithm, phase region expanding labeller for unwrapping discrete estimates (PRELUDE) from FSL package (23). This algorithm also applies a brain mask from magnitude image to extract brain tissue.

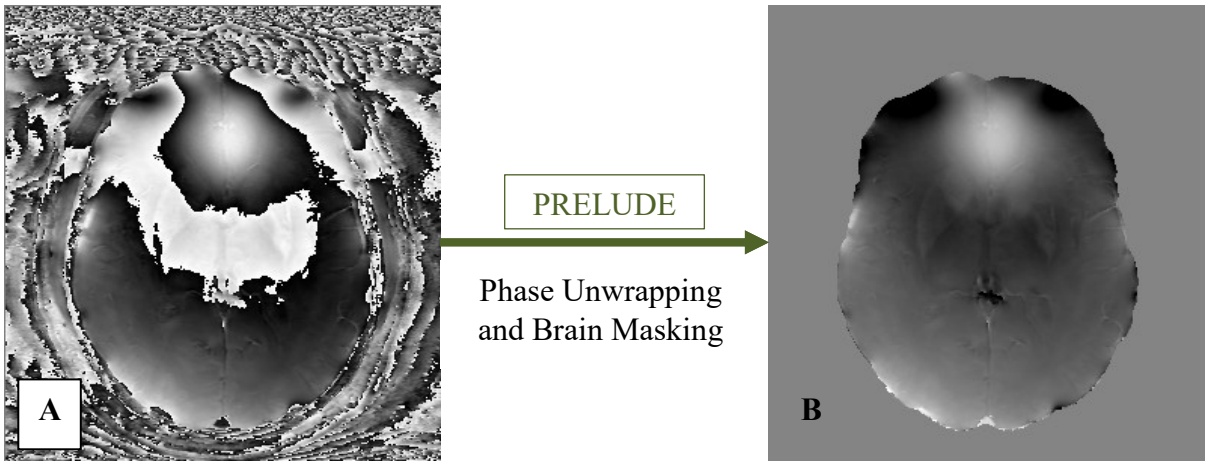

Figure 9 Phase before and after Unwrapping

1.4.3. Generating Brain Masks

The next important step in creating magnetic susceptibility maps is generating a binary brain mask from magnitude images to extract the brain from skull and segment the region of interest for background field removal step. Noisy regions such as areas near air-

tissue interfaces induce erroneous local field changes and cause artifacts in susceptibility maps (19, 24). Therefore, the brain is usually extracted, for example by using brain extraction tool (BET) from the FSL package (25). Figure 10 shows the binary brain mask and extracted brain using the mask.

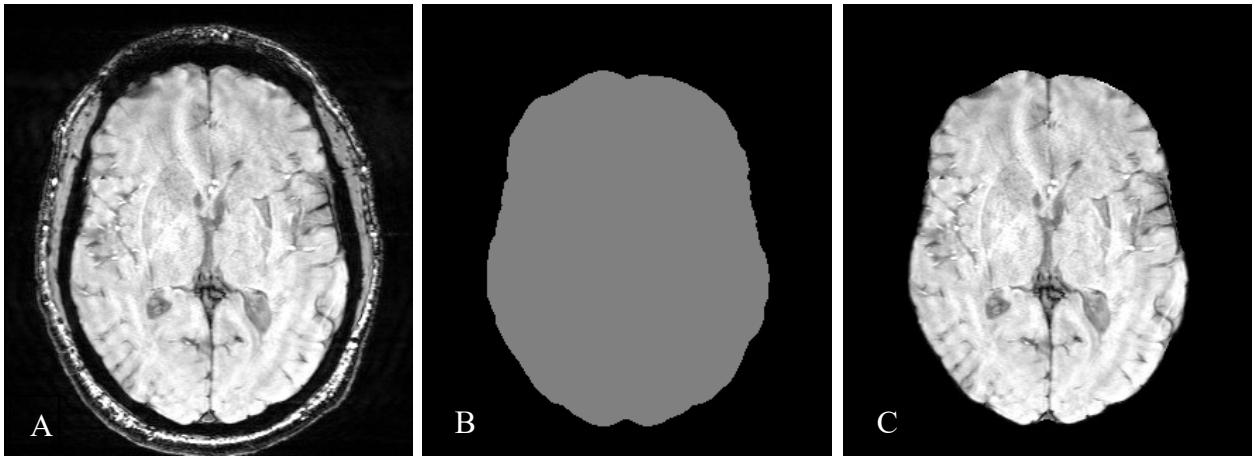

Figure 10 Brain extraction. Magnitude image (A). Binary brain mask created by BET tool (B). Extracted brain (C).

1.4.4. Background Field Removal

The field perturbation, $\Delta Bz(\vec{r})$, is a sum of local field variations that are induced by local susceptibility distribution and background field that is due to air-tissue interfaces, any field inhomogeneity and chemical shift. To obtain the local susceptibility distribution by using the field-to-susceptibility equation, the contribution of background field needs to be removed:

$$B_{Local} = B_{Total} - B_{Background} \quad (1.13)$$

This critical process of QSM is called background field removal. Figure 11 shows total, local and background field.

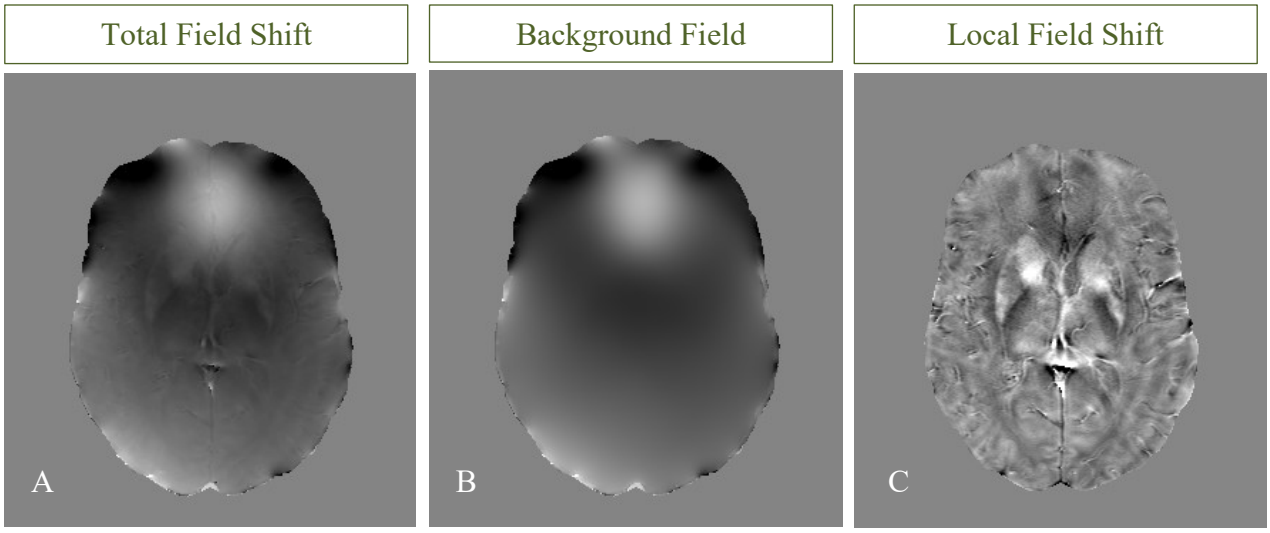

Figure 11 Total measured field is a summation of dominant macroscopic background field and the microscopic local field.

There have been several methods proposed for this process including high-pass filtering, projection onto dipole fields (PDF), regularization-enabled sophisticated harmonic artifact reduction for phase data (RESHARP).

1.4.4.1. High-Pass Filtering

Background field can be considered as slow varying and therefore high-pass and homodyne filters have been used to remove the unwanted background field and preserve the local field (26). However, this method is unsuccessful in removing high frequency components of background field near the tissue boundaries and also erroneously removes the low frequency components of the local field (27).

1.4.4.2. Projection onto Dipole Fields

This approach assumes the background field to be originating from dipole sources outside the brain that are projected onto the brain. By knowing the fact that magnetic field for dipoles outside the brain is perpendicular to the magnetic field of dipoles inside, one can estimate the local field distribution by finding a background susceptibility distribution that can create the total field inside the brain tissue most closely (28). Local field can then be derived by:

$$B_{Local} = B_{Total} - B_{Estimated\ Background} \quad (1.14)$$

PDF method does not count for susceptibility sources that are not outside the brain, such as B_0 inhomogeneities caused by imperfect shimming and would require application of other methods like HPF to remove the remaining background field.

1.4.4.3. Regularization-Enabled Sophisticated Harmonic Artifact Reduction for Phase Data (RESHARP)

Maxwell's equations show that the susceptibility sources outside the ROI induce harmonic dipole field across the ROI. With considering mean value property as one of the properties of harmonic functions, we would have:

$$\Delta B_b(\vec{r}) * s = \Delta B_b(\vec{r}) \quad (1.15)$$

Where 's' is a normalized spherical kernel. Using Equation 1.13 and substituting $\Delta B_b(\vec{r})$:

$$\Delta B_z(\vec{r}) - \Delta B_z(\vec{r}) * s = \Delta B_l(\vec{r}) - \Delta B_l(\vec{r}) * s = \Delta B_l(\vec{r}) * (\delta - s) = \Delta B'(\vec{r}) \quad (1.16)$$

This statement can be named $\Delta B'(\vec{r})$ for simplicity. Since there may be no reliable phase data available for regions that are within a distance of *R*, the radius of the spherical kernel, from the edge of the brain (29); the convolution results may not be correct for these regions. Therefore, an eroded brain mask is applied to $\Delta B'(\vec{r})$ to confine the $\Delta B'(\vec{r})$ to the regions with valid data. Then, $\Delta B_l(\vec{r})$ can be calculated by performing a deconvolution:

$$\Delta B_l(\vec{r}) = \Delta B'(\vec{r}) * (\delta - s)^{-1} \quad (1.17)$$

$(\delta - s)^{-1}$ is the regularized inverse kernel. Size of this kernel and the spherical kernel determines the accuracy of this method, which is called sophisticated harmonic artifact reduction for phase data (SHARP).

The brain mask used in this method, assumes that there is no susceptibility source close to the boundary and this, causes artifacts (30). Also, SHARP and other previously

mentioned methods, generally remove the harmonic components of non-internal sources such as phase offsets related to B_1 but are not successful in eliminating the non-harmonic components. These components would be erroneously calculated as internal field variations. Sun proposed the regularization-enabled SHARP (RESHARP) (31) that uses Tikhonov regularization in formulating the background field removal as an optimization problem. This method allows suppression of non-harmonic components and although it eliminates the contribution of non-internal sources, it might remove the non-harmonic components of the local field as well. Overall, it has been shown to be more successful than SHARP in producing more reliable results near the boundaries, when same spherical kernel is used (31).

1.4.5. Susceptibility Inversion

As mentioned in section 1.4.1, due to the singularity cones in the unit dipole kernel, the susceptibility inversion from field perturbation is an ill-posed problem and cannot be directly calculated by simple inversion of field changes over dipole kernel. Various methods have tried to offer solutions that will be explained in the subsequent sections.

1.4.5.1. Multiple Orientation Method

We know that the two cones of zero in the dipole kernel $G(\vec{k})$, are at the magic angle of 54.7° where $k_x^2 + k_y^2 = 2k_z^2$. To reconstruct a pristine susceptibility map, the object can be scanned in different orientations and the data can be combined to mask out the zero-cone areas. This method is known as calculation of susceptibility through multiple orientation sampling (COSMOS) (32).

In clinical applications, this method is not practical considering the fixed direction of main magnetic field and the design of head coils leaving less room for head movements to maximize the SNR. In addition, the multiple acquisitions would increase the scan time.

1.4.5.2. Truncated k-space Division (TKD)

The zero cones and low values of $G(\vec{k})$ make the inversion process erroneous and amplify the noise. A simple solution is to truncate the dipole kernel and restrict the $G(\vec{k})$ to

have a minimum value of t, a user-defined threshold (9, 33). This approach keeps the inverse of $G(\vec{k})$ well-defined:

$$\tilde{G}(\vec{k}) = \begin{cases} \mathrm{G}(\vec{k}) & |\mathrm{G}(\vec{k})| > t \\ sgn\,(\mathrm{G}(\vec{k})).t & |\mathrm{G}(\vec{k})| < t \end{cases} \quad (1.18)$$

$\tilde{G}(\vec{k})$ will then be used in the dipole inversion equation:

$$\chi(\vec{k}) = \frac{1}{\tilde{G}(\vec{k})} \frac{\Delta \mathrm{Bz}(\vec{k})}{B_0} \quad (1.19)$$

The solution is time-efficient and can be used for data from single orientation scans; however, it leads to underestimation of susceptibility values and causes streaking artifacts in the reconstructed images. Proper selection of threshold value, acts as a trade-off between level of streaking artifacts and the underestimation of susceptibility values (9, 19).

1.4.5.3. Total Variation

Image regularization methods have also been proposed as solutions for dipole inversion. Regularizations in QSM are mostly expressed as optimization problems:

$$\Delta\chi(\vec{\mathrm{r}}) = \mathrm{argmin}_{\Delta\chi(\vec{\mathrm{r}})} ||\mathrm{W}[\Delta \mathrm{B_z}(\vec{\mathrm{r}}) - \mathrm{B_0}\Delta\chi(\vec{\mathrm{r}}) * \mathrm{G}(\vec{\mathrm{r}})]||_2^2 + \lambda\,.\,\mathrm{R} \quad (1.20)$$

W is a weighting function and R is the regularization term. R can be constructed from different a priori information such as features of susceptibility distribution or magnitude images. The mostly used form of regularization terms are L1 and L2 norms with L1 norm being proved to be more advanced with greatly diminished streaking artifacts compared to those using L2 norm for reconstruction and better suppression of background noise (34). Total variation (TV) (35, 36) can be stated as an example that exploits L1 norm of susceptibility gradients. This method assumes the susceptibility distribution to be piece-wise and hence, with gradients (sparse edges). Compressed sensing (CS) (37) theory suggests that if an image is sparse in a transform domain, it can be recovered from under-sampled k-space data. By assuming the susceptibility distribution to be sparse, it can be reconstructed from k-space.

Magnitude images are widely used as a priori information, however in situations that edges in magnitude and susceptibility distributions do not match e.g. large blooming artifacts due to hemorrhages on T_2*-weighted magnitude images, this method should be used with caution as it might yield in inaccurate estimate of susceptibility distribution.

1.4.6. Clinical Application of QSM

QSM can discriminate between diamagnetic and paramagnetic sources, and is therefore able to differentiate between iron-containing lesion versus calcification (17, 38, 39) and detect tissue changes in multiple sclerosis (MS) patients (40, 41). It has also been examined to study stroke patients (42, 43), measure vein oxygenation and other clinical applications (44-46). In the following, some of these applications will be discussed in detail, while stroke and cerebral microbleed (CMB) detection, as the main clinical applications studied in this work will be covered in the next chapters.

1.4.6.1. Quantification of Iron in Brain

Ex-vivo examinations of a number of neurodegenerative diseases such as MS (47), Alzheimer's (47, 48) and Parkinson's (49, 50) disease, and neurodegenerative brain iron accumulation (51) has shown increased iron levels in the basal ganglia and thalamus. This phenomenon also happens in healthy aging of the brain (52). Due to paramagnetic properties of iron, QSM is highly sensitive to iron accumulations in grey matter and provides an in vivo tool for detection and quantification of iron levels in Parkinson's (53, 54), Alzheimer's (55) and monitoring MS disease progression (41, 56-59), healthy aging (35) and intracranial hemorrhage (60).

1.4.6.2. Oxygenation

For brain tissue to maintain functionality and viability, continuous oxygen delivery is necessary. Noninvasive oxygenation imaging could provide metabolic biomarkers to study cerebral physiology and help us understand disorders in which the oxygen saturation varies from normal level, such as stroke.

Oxygen extraction fraction (OEF) can be calculated by measuring the susceptibility difference between veins and tissue:

$$\Delta X_{vein-tissue} = \Delta X_{do} \times Hct \times OEF \quad (1.21)$$

Hematocrit (Hct) is the percent of blood that consists of erythrocytes and ΔX_{do} is the susceptibility difference per hematocrit (Hct) between fully oxygenated blood and fully deoxygenated blood (61). During metabolic oxygen consumption in tissue, weakly diamagnetic oxyhemoglobin becomes strongly paramagnetic after releasing O_2.

Cerebral metabolic rate for oxygen ($CMRO_2$) can also be obtained according to Fick's principle of arteriovenous difference:

$$\mathrm{CMRO_2} = \mathrm{OEF} \times \mathrm{CBF} \times \mathrm{C_a} \quad (1.22)$$

Where C_a is a constant representing carrying capacity of oxygen molecules per volume of blood and cerebral blood flow (CBF) can be measured by MRI methods like arterial spin labeling (62).

A number of studies have assessed QSM for estimation of oxygen extraction directly from veins in healthy volunteers (61, 63) and human fetus (64). Xia and others studied 26 acute ischemic stroke patients who had asymmetrically prominent cortical veins (APCV) in the infarcted region (42). They aimed to test the hypothesis of correlation of APCVs with oxygenation. They obtained the blood oxygen saturation level from the susceptibility difference by using equation 1.21.

Also, several studies compared the QSM measurements with results from previous work based on other MRI methods or positron emission tomography (PET) (62, 65, 66).Overall, results show that QSM can be used not only to visualize veins but also to measure OEF and provide valuable and reliable in vivo information regarding cerebral physiological changes.

1.5. Overview of Thesis

With the key MRI concepts now introduced in Chapter 1, Chapter 2 will provide clinical background on stroke and microbleeds. Chapter 3 then provides the main study of this thesis which examines the value of QSM in ischemic stroke. The hypothesis of this thesis is that QSM can provide a comprehensive evaluation of ischemic stroke, providing information on tissue and vein oxygenation and microbleeds.

2. Stroke and Cerebral Microbleeds

2.1. Stroke

2.1.1. Introduction

Stroke is a leading cause of death and disability in the world (67, 68). It occurs due to reductions in blood flow to the brain (61). Interrupted circulation of blood flow and therefore obstruction in delivery of oxygen and nutrition to the brain, causes irreversible pathological injuries to the tissue. These interruptions could be due to either narrowing and blockage (ischemic type) or rupture (hemorrhagic type) of cerebral arteries (Figure 12).

In the subsequent sections, two types of stroke are elaborated. Since the focus of this thesis is on ischemic stroke, imaging methods utilized for this specific type are discussed in the following section.

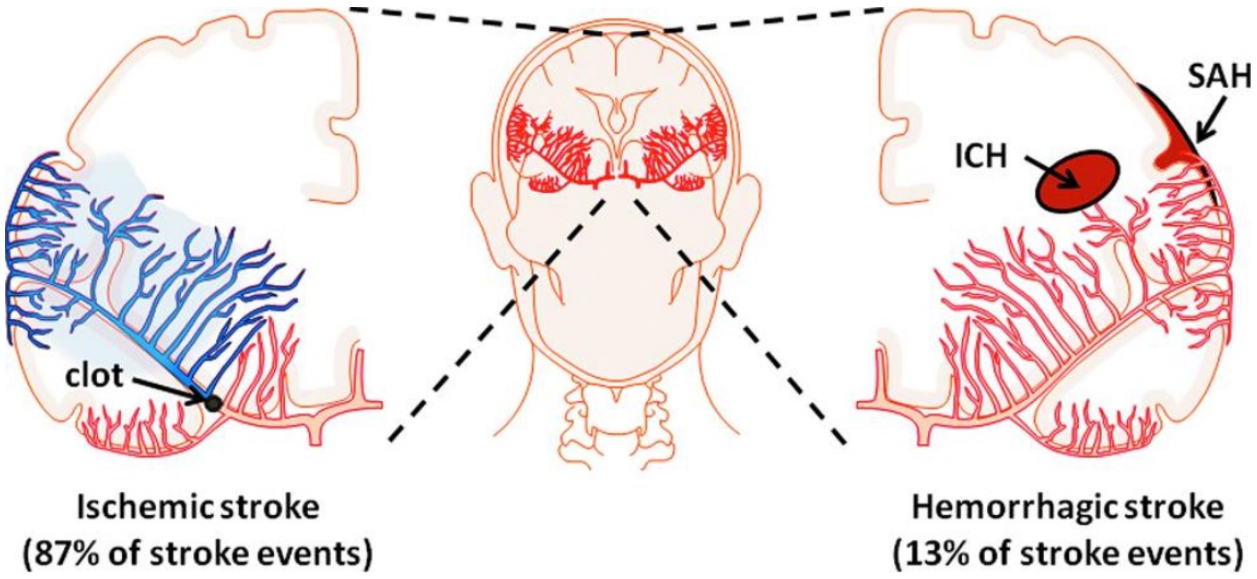

Figure 12 Demonstration of two etiological origins of stroke: ischemia (left) and hemorrhage (right). Ischemic stroke can be due to a clot or narrowing in cerebral artery. Hemorrhagic stroke occurs as a result of hemorrhage in intracerebral space (ICH) or subarachnoid space (SAH). (Cameron Rink and Savita Khanna. Antioxidants & redox signaling. 2011)

2.1.2. Ischemic Stroke

Ischemic stroke counts for roughly 80% of all stroke cases. It can be divided into two main types of embolic and thrombotic. Embolic type is when the blood clot (emboli) created within an artery are formed somewhere else in the body other than brain, and travel with the bloodstream until they cannot go any further and cause the blockage. Thrombotic strokes are caused by blood clots within the brain arteries. Thrombotic stroke can be classified further into subgroups depending on the location of thrombosis, in large-vessels, like carotid middle cerebral artery, or small-vessels (also named lacunar infarction).

These blood clots can usually originate as a result of accumulated fat in the wall of blood vessels, known as atherosclerosis (69-71).

2.1.3. Hemorrhagic Stroke

Hemorrhagic strokes are primarily categorized as intracerebral (ICH), or subarachnoid (SAH) hemorrhages, based on the location of hemorrhage. ICH is the condition that bleeding occurs within the brain tissue. It can happen due to reasons such as tumors, ischemia, trauma and aneurysms (72, 73). ICH counts for 10-15% of all strokes (73, 74), but contributes to significant morbidity and mortality (75).

On the other hand, SAH is when bleeding happens at the base of the brain and leading to an extravasation of blood into the subarachnoid spaces that are filled with cerebrospinal fluid (76). Case fatality for this type of stroke is ~50% overall with one third of survivors remaining dependent (77).

2.1.4. Ischemic Stroke Imaging

Brain imaging plays a crucial role in initial evaluation and other stages of stroke disease. Brain images can provide information about the location and size of the infarct, vascular distribution in the infarcted region, severity of the ischemic stroke, vessel status (location of occlusion and the severity), cerebral perfusion and salvageable tissue (78, 79) . For an early diagnosis of stroke, non-contrast enhanced computed tomography (NECT) is the most commonly-used method. Despite its relative insensitivity to acute small cortical and

subcortical infarcts (80, 81) and lower sensitivity in detection of acute stroke/ ischemic stroke compared to MRI (82), advantages such as immediate availability in clinics, acquisition speed, ease of interpretations and sensitivity to intracranial hemorrhage make this method the initial scan in stroke routine (79). CT angiography (CTA) with iodinated contrast agent is employed to detect stenoses and occlusions within the vasculature system (83).

MRI sequences are also clinically used for diagnosis of acute ischemic stroke and detection of infarcts. While standard sequences such as T_1 and T_2-weighted are not very sensitive to ischemia, diffusion-weighted imaging (DWI) has been increasingly used in clinical trials for its ability to detect and identify the location and size of the ischemia with high sensitivity and accuracy compared to CT imaging that can help in understanding the evolution and outcome of stroke (84-90).

Furthermore, other MRI methods such as angiography (two types: time of flight (TOF) and contrast enhanced MRA) are employed with combination of other methods to provide information on vascular distribution and location of occlusion (91).

Recently, other MRI methods such as SWI have also been used for vein oxygenation analysis and depiction of hypointense veins (42, 92-94). Xia and others studied cortical veins in infarcted and contralateral hemisphere among 26 acute ischemic stroke patients who had APCV in the infarcted region (42). They observed a significantly higher susceptibility of the APCVs in the stroke hemisphere compared to the contralateral hemisphere and in healthy controls. They also found that this susceptibility difference correlates with a decrease in oxygen saturation in APCVs relative to cortical veins in the contralateral hemisphere. Patients selected for this study had APCV and susceptibility variations in cortical veins of other ischemic stroke patients without APCV was not assessed in this work.

QSM has also been employed to provide quantified measures of oxygenation (42). These pieces of information are valuable in the diagnosis and prognosis of stroke, but further study is needed. In particular, past studies on ischemic stroke have focused on large strokes and a wider range of strokes should be studied, as will be undertaken here.

2.2. Cerebral Microbleed

2.2.1. Introduction

Cerebral microbleeds (CMBs), also called micro-hemorrhages are small brain hemorrhages caused by blood leakage from small brain vessels (95, 96) that are depicted as round/oval parenchymal hypointense regions on gradient echo, T_2* and susceptibility-weighted images due to the paramagnetic properties of blood-degradation product deposits (hemosiderin, deoxyhemoglobin and methemoglobin) in the brain (96). These blood deposits causes a local increase of magnetic field in surrounding tissue resulting in signal loss on images (95, 96). Cerebral microbleeds are prevalent in cerebrovascular diseases and studies suggest them as risk factors for intracerebral hemorrhages (97-99) and cardiovascular diseases (100). They have been examined in different pathologies such as Alzheimer's disease (101), dementia (102, 103) and traumatic brain injury (104).

The paramagnetic property of blood-breakdown product in CMBs, results in a signal drop out on T_2*-weighted GRE images. SW images have been shown to provide a better contrast of microbleeds due to the sensitivity of this sequence to susceptibility sources (96). Furthermore, this sequence can differentiate between microbleeds and calcification (105). However, the blooming effect on SWI and T_2*-weighted GRE images, characterizes CMBs different than their actual size (96, 105).

Recently, QSM has been assessed for better quantification of microbleed size compared to standard MRI methods such as T_2*-weighted and SWI (95, 96, 105). QSM enabled removal of blooming artifacts, stability across echo times and better distinction between calcium, air and actual bleeds.

2.2.2. Segmentation

General agreement is that microbleeds are areas of signal void on T_2*-weighted GRE images with the diameter range of 2 mm to 10 mm. However, due to the blooming artifact on

GRE and SW images, there should not be an emphasis on the precise size criteria (96, 106). Another complication of CMB detection is that both calcium and iron deposits appear as small hypointense areas on T_2*-weighted images, this problem can be addressed by SWI sequence, which differentiates between dia- and paramagnetic materials.

Microbleeds can be detected by visual inspection on susceptibility-weighted images. To segment and measure the size of microbleeds, some studies have used full width at half maximum (FWHM) of the profile as the diameter of the microbleed (95, 107) and this method has been employed in this study as well.

3. Quantitative Susceptibility Mapping to Detect Microbleeds and Measure Vascular and Tissue Oxygenation in Patients with Ischemic Stroke [1]

3.1. Abstract

Background and Purpose:

Susceptibility-weighted imaging (SWI) is often used in ischemic stroke follow-up for microbleed or hemorrhage detection. A new form of SWI reconstruction enables quantitative susceptibility mapping (QSM). This method may enable measures of tissue and vein oxygenation as well as microbleed detection. Here we examine these three features of QSM in ischemic stroke patients.

Methods:

Twenty acute ischemic stroke patients with mild (NIHSS ≤5) (63% male, mean age = 71.7±14.2 years) or severe stroke (NIHSS> 5) (33% male, mean age= 66.2 ± 17.6 years) were selected for the oxygenation study. Nineteen chronic stroke subjects (63% male, mean age= 70.5±11.5 years) had evident microbleeds and were selected for the microbleed study. All subjects received susceptibility-weighted imaging, which was reconstructed into QSM. The susceptibility maps from each acute group were analyzed to detect susceptibility differences in vein and brain tissue between infarcted and homologous contralateral regions. Microbleeds were detected on SWI and compared with QSM.

Results:

Results showed significantly higher susceptibility in ipsilateral major ($p< 0.001$) and local veins ($p< 0.002$), and white matter ($p< 0.036$) compared to the contralateral hemisphere among both mild and severe stroke patients. Cerebral microbleeds had distinct contrast on QSM and smaller area measurements compared to SWI and magnitude images ($p< 0.0001$) due to elimination of blooming effects.

Conclusions:

[1] This chapter is being prepared for journal submission.

Visualization of microbleeds, and significant susceptibility differences of veins and tissue in ipsi- and contralateral regions provide a unique role for QSM in ischemic stroke studies, requiring only the raw phase images from SWI studies.

3.2.Introduction

Magnetic Resonance Imaging plays a crucial role in small infarct detection (108, 109) and ischemic stroke follow up (86, 110). A common addition to clinical MRI protocols for ischemic stroke is susceptibility-weighted imaging (SWI) (12), which enables detection of cerebral microbleeds and hemorrhage (111). Using the raw phase images from SWI, magnetic susceptibility maps may be generated using an emerging MRI post-processing technique named quantitative susceptibility mapping (QSM) (22, 29). Similar to SWI, QSM is highly sensitive to paramagnetic iron found in various states of blood from deoxyhemoglobin to hemosiderin.

The construction of QSM from SWI has been used for detection of microbleeds and larger hemorrhages (38), and may provide an additional measure to gauge hemorrhage age (60). Cerebral microbleeds , also called micro-hemorrhages are prevalent in cerebrovascular diseases and studies suggest they are risk factors for intracerebral hemorrhage (97-99, 112) and cardiovascular disease (100). They have been examined in different pathologies such as Alzheimer's disease (101), dementia (102, 103) and traumatic brain injury (104). Non-SWI sequences, such as multiple-echo gradient echo, have also been used for QSM of hemorrhage (113).

Tissue and vein oxygenation level in brain is a prominent parameter in determining the severity of ischemia and tissue viability (114). Due to its sensitivity to deoxyhemoglobin, QSM provides a quantitative measure of brain oxygenation in tissue or in veins (33, 42, 61, 63, 64, 66, 115, 116) and can provide a quantitative measure of oxygen extraction fraction (OEF) as a crucial marker of tissue viability. Recent work in ischemic stroke has demonstrated differences in QSM between ipsilateral and contralateral hemispheres and in veins (42, 66, 115, 116). However, these studies only examined severe ischemic strokes (such as middle cerebral artery (MCA) occlusion). There are no studies to date that examine all three potential applications of QSM to ischemic stroke: cerebral microbleed

quantification, and vein and tissue oxygenation. Thus, our study investigates the value of QSM in ischemic stroke patients with a wide range of stroke severity, by evaluating susceptibility change in tissue and draining veins from infarcted and contralateral regions in acute ischemic stroke and assessing microbleed burden in comparison to standard SWI in chronic stroke.

3.3. Material and Methods

3.3.1. Patient study

Patients suspected or diagnosed with transient ischemic attack (TIA) or ischemic stroke were prospectively examined with MRI between January 2016 and May 2018 (Figure 13), from two clinical trials.

The initial purpose of patient selection and data collection for the first trial was to investigate the hypothesis that symptomatic hemorrhagic transfer rates in dabigatran, a novel oral anticoagulant agent, and ASA, acetylsalicylic acid – current standard of care, treated patients will not be significantly different. The criteria for that study was:

Inclusion Criteria:

1. Male or female patients
2. Must be >18 years of age
3. Must have TIA or ischemic stroke (national institute of health stroke scale (NIHSS) score <9)
4. Symptom onset is < 72 hours prior to enrollment or Study therapy must initiated within 48 hours of symptom onset (in case where onset time cannot be established, it will be considered to be the time when the patient was first known to be well)
5. Informed consent must be obtained from either the patient or substitute decision maker (according to local research ethics board policy) prior to any study related procedures being performed

6. All patients will have a MRI including DWI prior to randomization
7. DWI lesion volume must be <25ml
8. Patients without DWI lesions, but a clinical history considered consistent with TIA, determined by the attending physician, can be included

Exclusion Criteria:

1. Patients with stroke mimics - such as seizures, migraine etc.
2. Patients with contraindications to MRI including metallic implants
3. Patients with any past sensitivity to gadolinium contrast media will be eligible, but will not undergo PWI or contrast enhanced MRA (both optional sequences)
4. Patients with renal failure defined as Glomerular Filtration Rate (GFR) < 30 ml/min
5. Patients deemed, as attending stroke physician, to have any ongoing bleeding risks or unsuitable for dabigatran therapy
6. Patients with MRI demonstrated additional pathology including arteriovenous malformations, intracranial aneurysms, tumors or abscess, which potentially increase the rise of bleed. Individuals with small incidental lesions, at low risk of bleed such as meningiomas may be included at the discretion of the investigator.
7. Patients with an acute DWI lesion volume of >25 ml
8. Age <18 years
9. Pregnant or breast-feeding women.
10. Severe dysphagia necessitating naso-gastric (NG) feeding (dabigatran cannot be delivered via NG tube)
11. Planned thrombolysis or endovascular intervention for the index event

12. Thrombolysis for ischemic stroke within the preceding 7 days
13. Planned carotid endarterectomy/carotid artery stent within 30 days Note: Carotid Investigations will be completed prior to enrolment. Patients with symptomatic stenoses and a planned carotid procedure will be excluded.
14. Any history of spontaneous intracranial bleeding
15. Clear indication for anticoagulation, including atrial fibrillation, mechanical cardiac valves, deep venous thrombosis, pulmonary embolism or known hypercoagulable state
16. Co-morbid illness with expected life expectancy of <90 days

The study was approved by the local ethics committee and written informed consent was obtained.

The purpose of the second trial, was to test the hypothesis that a small acute perfusion lesion predicts good clinical outcome regardless of thrombolysis administration, since despise being commonly used in clinical practice, there remains much uncertainty about whether perfusion computed tomography (CTP) should be used to select stroke patients for acute reperfusion therapy (117). Clinical and imaging information from acute ischemic stroke patients presenting to the hospital within 12 hours of symptom onset were prospectively collected for the International Stroke Perfusion Imaging Registry (INSPIRE). The imaging information was baseline multimodal CT (NCCT, CTP, and CT angiography [CTA]), and follow-up imaging at 24 to 48 hours poststroke. At 24 to 48 hours after acute imaging, all patients, regardless of treatment, underwent a stroke magnetic resonance (MR) imaging protocol on 1.5 Tesla (T) or 3T scanners. The MR protocol included an axial gradient-echo T_2*-weighted series, diffusion-weighted imaging (DWI), MR time of flight angiography, perfusion-weighted imaging, and fluid-attenuated inversion recovery. Follow-up infarction was defined on DWI using automated signal intensity thresholds. Clinical stroke severity was assessed at the two imaging time points using the NIHSS score. Eligible patients were treated with intravenous thrombolysis according to local guidelines and the clinical judgement of the treating physician. Written informed consent was obtained from all participants for their information to be collected for the registry, and the INSPIRE study was approved by the

local ethics committees in accord with Australian National Health and Medical Research Council guidelines.

Two patient groups from these two trials were considered: Group 1 included 38 patients suspected of having an ischemic stroke examined in the first days after symptom onset for tissue and vein QSM measurements. Group 2 involved 124 suspected stroke patients examined 30 days after symptom onset to examine cerebral microbleeds. Inclusion criteria for Group 1 patients were an evident infarct on diffusion-weighted images and no major artifacts on SWI, yielding 20 subjects (Table 1). The twenty patients were divided into two subgroups of mild or severe stroke based on the NIHSS score. Subgroup A included 11 patients (7 males, mean age = 71±14 years) with mild stroke (NIHSS score ≤ 5) and NIHSS:2.1 ± 1.6) Subgroup B included 9 patients (3 male, mean age= 66 ± 17 years and NIHSS:12.8 ± 4.5) with severe stroke (NIHSS score > 5). Patients in Group 2 were included if cerebral microbleeds were evident on SWI, yielding 19 subjects (12 male, mean age= 70 ± 11 years) with a total of 116 evident microbleeds.

Table 1A, B Subject demographics for stroke patients (left: mild stroke patients, right: severe stroke patients)

Patient Number	Age (years)	Sex	Symptom onset to scan time (hours)	NIHSS	Lesion Volume on DWI (mL)	Age (years)	Sex	Symptom onset to scan time (hours)	NIHSS	Lesion Volume on DWI (mL)
1	90	M	6	2	0.4	62	F	19	11	4.2
2	53	M	5	1	0.5	78	M	15	8	11.9
3	57	M	5	0	0.7	87	F	38	11	25.2
4	91	F	66	1	1.4	89	F	47	23	38.2
5	84	M	41	3	1.8	64	M	35	11	52.5
6	62	F	18	5	25.7	41	F	41	8	55.7
7	65	F	59	3	35.9	58	F	50	17	64.7
8	61	M	16	0	5.1	79	F	46	11	81.8
9	57	M	27	1	8.5	38	M	100	15	172.2
10	87	M	28	3	10.5	-	-	-	-	-
11	82	F	24	4	16.0	-	-	-	-	-
Mean	71		26	2.09	9.7	66		43	12	56.3
SD	14		19	1.56	11.2	17		23	4	47.3

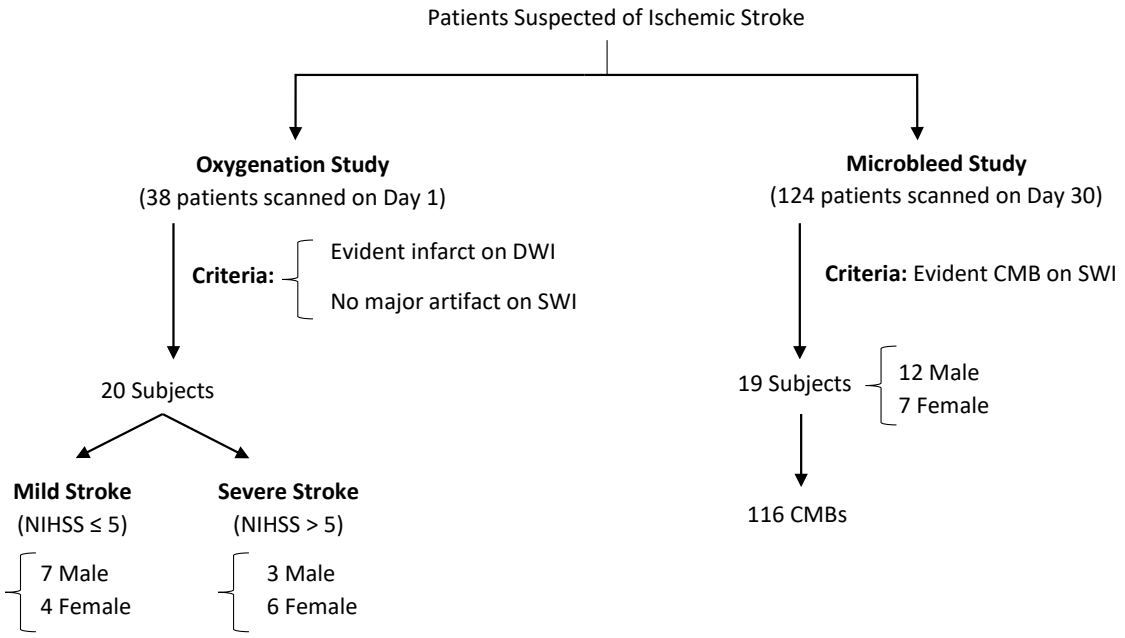

Figure 13 Subjects' demographic information

3.3.2. MRI Methods

The imaging protocol included DWI, SWI, arterial spin labeling (ASL), fluid attenuated inversion recovery (FLAIR), T_2-weighted imaging, time of flight (ToF), perfusion weighted imaging (PWI), SWI echo planar imaging (SWIEPI) and volumetric T_1-weighted imaging with total imaging time of 32 minutes, acquired on a 3T (Prisma Siemens). The 3D SWI sequence used for QSM used the following parameters: TR/ TE 28ms/ 20ms, flip angle 15°, voxel size 0.7×0.7×2.0 mm^3, number of slices 72, in-plane matrix size 290 × 320 and imaging time 3:32 minutes. Parameters were selected according to the clinically used SWI sequence. SW images were reconstructed to produce the magnitude and raw phase images for QSM reconstruction. Fractional anisotropy (FA) and mean diffusivity (MD) maps were also produced from DWI. Parameters for other sequences are listed in the following:

DWI: TR/ TE 7900ms/ 57ms, b=0, 1000, voxel size 0.7×0.7×1.5 mm^3, number of slices 80, and imaging time 3:59 minutes.

ASL: TR/ TE 4600ms/ 18.ms, voxel size 2.0×2.0×2.0 mm^3, one slab, number of slices in one slab 40, and imaging time 3:45 minutes.

FLAIR (sagittal): TR/ TE 5000ms/ 385ms, inversion time (TI) 1800ms, voxel size 1.2×1.2×1.2 mm^3, number of slices 160, and imaging time 3:07 minutes.

T2-weighted (sagittal): TR/ TE 3200ms/ 409ms, voxel size 1.2×1.2×1.2 mm^3, number of slices 160, and imaging time 2:10 minutes

T1-weighted (sagittal): TR/ TE 1800ms/ 2.37ms, flip angle 8°, voxel size 0.9×0.9×0.9 mm^3, number of slices 208, and imaging time 3:39 minutes

ToF: TR/ TE 21ms/ 3.43ms, flip angle 18°, voxel size 0.3×0.3×0.5 mm^3, four slabs, 40 slices per slab, and imaging time 5:33 minutes. Also, 30 slices per slab with 3 slabs, voxel size 0.3×0.3×0.75 mm^3 with imaging time of 3:13 minutes.

PWI: TR/ TE 1700ms/ 30ms, flip angle 90°, voxel size 0.8×0.8×5.0 mm^3, number of slices 24, and imaging time 1:49 minutes.

SWIEPI: TR/ TE 6040ms/ 25ms, flip angle 82°, voxel size 1.5×1.5×1.5 mm^3, number of slices 80, and imaging time 0:24 minutes.

All images were spatially registered for further analysis using FMRIB's linear image registration tool (FLIRT) (118).

3.3.3. Data Processing and Analysis

QSM Reconstruction

QSM images QSM images were reconstructed from raw phase images, using phase region expanding labeller for unwrapping discrete estimates (PRELUDE) to perform phase unwrapping (23), brain extraction tool (BET) from FSL package to extract brain tissue (25), regularization-enabled sophisticated harmonic artifact reduction for phase data (RESHARP) for background field removal (31) (kernel radius = 3mm, Tikhonov regularization parameter =0.001) followed by dipole inversion with total variation (TV) regularization (TV parameter =0.0005).

Vein Measurements

Regions-of-interest (ROIs) for major draining veins (such as great cerebral vein, straight sinus, internal cerebral vein, Basilar vein and inferior sagittal sinus) and local veins within the infarct territory and the homologous contralateral region were drawn manually on SW images using ImageJ. Susceptibility measurements were performed for both major veins (such as inferior sagittal sinus, straight sinus and internal cerebral sinus) and the local veins in the infarcted hemisphere as well as the veins in the contralateral region over the slices that contained the infarct on QSM images.

Tissue Measurements

For QSM measures from infarcted tissue, ROIs were drawn on one slice based on signal hypo-intensity on DWI images in the ipsilateral affected hemisphere and in the homologous contralateral region using ImageJ. Separate ROIs for grey and white matter were segmented using DWI and MD maps to identify the lesion and volumetric T_1-weighted images and FA maps to provide enhanced grey-white matter contrast (119). The regions were also checked on minimum Intensity Projection (mIP) SW images (mIP over all slices where a DWI hyper-intensity was visible) to ensure veins did not contribute to the signal within that ROI.

Cerebral Microbleeds

Cerebral microbleeds were defined to be small, oval, hypo/ hyper-intense lesions on SWI/ QSM images. Microbleeds were detected manually as hypo-intensities on SWI and hyper intensities on QSM which both provide distinction from calcification (120). Veins were differentiated from cerebral microbleeds based on their continuity along/ across slices. Area and mean QSM value were measured for each microbleed on twice interpolated images on QSM, SW and magnitude images.

3.3.4. Statistical Analyses

Statistical analyses were performed with “GraphPad Prism Software, Version 7.05 for Windows, La Jolla California USA, www.graphpad.com”. The normality of data was tested

by histogram and the D'Agostino-Pearson omnibus normality test. Median [25%, 75%] format and nonparametric Spearman's correlation and Wilcoxon matched-pairs signed rank tests were used to display, analyze and assess correlation of the non-normally distributed data from microbleeds and also for the tissue and vein analysis, due to the relatively small sample size.

3.4. Results

Tissue and Vein Measurements

Figure 14 shows regions for the infarct and homologous contralateral region, and selected ROIs for local veins and major veins on DWI, SWI and QSM for a patient diagnosed with ischemic stroke. Table 2, 3 show the raw data measurements for both subgroups A and B. The statistical analysis of these tissue susceptibility measurements (in ppb) in infarcted and contralateral regions for Subgroups A and B are brought in Tables 4 and 5, respectively. Deoxyhemoglobin has paramagnetic properties (positive susceptibility) and higher susceptibility can be an indicator of less oxygenation. For tissue analysis, grey and white matter were analyzed separately to provide a more accurate detection of possible difference in susceptibility between infarcted and healthy hemispheres. Figure 15, 16 show selected ROIs for grey matter and white matter in two ischemic stroke patients. A total of 11, 12, 25 and 16 ROIs for subgroup A and 12, 10, 28, and 29 ROIs for subgroup B were identified for major veins, local veins, white matter and grey matter, respectively. For most of the patients, infarcts did not involve white matter and grey matter equally and this affected the number of possible ROIs (in both healthy and infarcted regions) from each patient.

Table 2 Raw data susceptibility measurements (in ppm) of white matter (WM) tissue, grey matter (GM), major veins and local veins in stroke versus control hemisphere for Subgroup A patients – mild stroke

Patient	Large vein		Local vein		Tissue WM		Tissue GM	
	Stroke hemisphere	contralateral hemisphere	Stroke hemisphere	contralateral hemisphere	Stroke hemisphere	contralateral hemisphere	Stroke hemisphere	contralateral hemisphere
1	0.181	0.096	0.065	0.048	-0.015	-0.027		
2	0.128	0.109	0.088	0.068			0.13	0.144
			0.08	0.07			0.114	0.13
3	0.095	0.066			-0.017	-0.0009175		
					-0.009	-0.007		
					0.008	-0.021		
4	0.122	0.09	0.05	0.03	-0.006	-0.028		
					-0.004	-0.024		
5	0.112	0.084	0.08	0.05	-0.011	-0.003		
					0.002	-0.002		
					0.007	-0.000517		
6	0.182	0.107	0.084	0.049	0.015	-5.82E-04	0.041	0.039
					0.019	0.024	0.011	-0.02
					-0.023	-0.022	-0.007	-0.035
							-0.001	0.032
							0.04	0.037
							-0.02	-0.007
							0.028	-0.019
							-0.018	-0.015
7	0.091	0.039	0.07	0.036	0.005	-1.30E-02	8.35E-04	0.006
					0.04	-0.038	0.012	0.006
					-0.024	-0.029	-0.002	-0.016
					-0.017	0.024	-0.009	0.028
8	0.28	0.211	0.14	0.113	-0.006	-0.007		
					0.024	-0.004		
9	0.173	0.107	0.063	0.045	-0.02	-0.024	0.008	-0.001
			0.084	0.076	-0.021	-0.026		
					-0.003	0.002		
					0.02	-0.005		
10	0.1	0.087	0.072	0.07	-0.039	-0.067		
					-0.021	-0.05		
11	0.127	0.051	0.086	0.05	-0.019	-8.36E-04	9.79E-04	9.17E-04

Table 3 Raw data susceptibility measurements (in ppm) of white matter (WM) tissue, grey matter (GM), major veins and local veins in stroke versus control hemisphere for Subgroup B patients – severe stroke

Patient	Large vein		Local vein		Tissue WM		Tissue GM	
	Stroke hemisphere	contralateral hemisphere	Stroke hemisphere	contralateral hemisphere	Stroke hemisphere	contralateral hemisphere	Stroke hemisphere	contralateral hemisphere
1	0.181	0.165	0.089	0.073			0.031	0.02
							0.026	0.02
2	0.138	0.103	0.062	0.042	-0.019	-0.033	0.027	0.026
					-0.041	-0.062	0.038	0.036
							0.088	0.06
							0.023	0.044
3	0.113	0.092	0.066	0.037	0.016	0.008	0.013	-0.004
					3.13E-04	-0.024	0.004	0.012
							0.008	-0.007
4	0.113	0.071	0.082	0.059	-0.014	-0.014	0.008	0.001
					-0.022	-0.024	0.009	0.002
							0.019	0.016
5	0.227	0.193	0.086	0.051	-0.014	-0.018	-0.007	-0.007
	0.185	0.135			-0.023	-0.026	-0.006	-0.011
					-0.012	-0.027		
					-0.013	-0.024		
6	0.122	0.053	0.056	0.038	-0.001	0.000552	-0.001	0.003
	0.098	0.039			-0.027	-0.08	-0.003	0.014
	0.103	0.085			-0.018	-0.017	-0.013	0.08
					-0.008	-0.011	-0.006	-0.005
7	0.131	0.097	0.125	0.077	0.012	2.00E-03	0.096	0.085
					-0.002	-0.006	0.096	0.093
					0.003	-0.007	0.054	0.047
					0.014	0.001	0.064	0.07
					-0.015	-0.013	0.012	0.01
8	0.103	0.088	0.029	0.014	0.007	-0.006	-0.012	-0.012
					0.007	-0.001	0.017	0.002
					-0.008	-0.0006	0.002	0.003
					0.001	-0.024	-0.011	-0.013
					-0.009	-1.00E-03	0.003	-0.007
					-0.015	-0.004		
					0.011	0.008		
9	0.129	0.108	0.075	0.03	0.006	-0.002	-0.004	-0.005
			0.119	0.053	0.003	-0.014		

The susceptibility measurements of local and major veins are significantly higher in infarcted hemisphere compared to the contralateral hemisphere among both subgroups ($p<$ 0.001 in patients with mild stroke and $p<$ 0.0001 in patients with severe stroke). The tissue assessment revealed a significantly higher susceptibility in white matter of the infarcted region in comparison to the homologous healthy region in both subgroups ($p<$ 0.036), while the significant difference in grey matter was not observed in either subgroup.

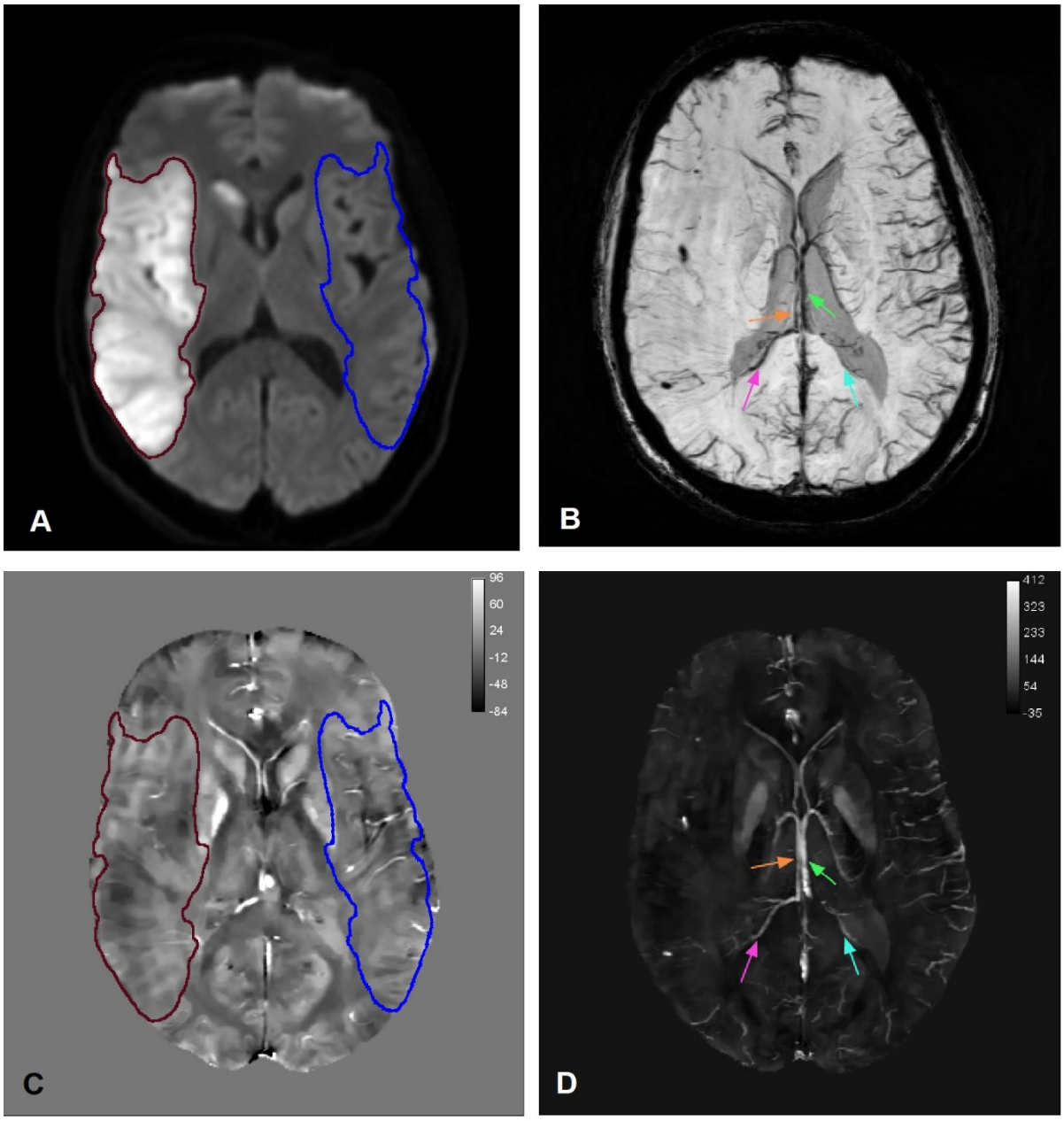

Figure 14 Images from an ischemic stroke subject: DWI (A), minimum Intensity Projection SWI (B), QSM (ppb) (C), Maximum Intensity Projection QSM to show veins (ppb) (D). Infarcted region (red) and homologous region(blue) are shown on DWI and QSM (A, C). Also, local veins (pink) and major veins (orange) in infarct territory and contralateral hemisphere (cyan for local vein and green for major vein) are depicted on mIP SWI and MIP QSM images (B, D). Also, note that in the infarcted region the tissue is destroyed, therefore it is likely that the tissue might not be getting as much perfusion/ the veins are dying/disappearing and hence fewer number of veins can be observed. The measurements were taken from present local veins in the infarcted region and contralateral region.

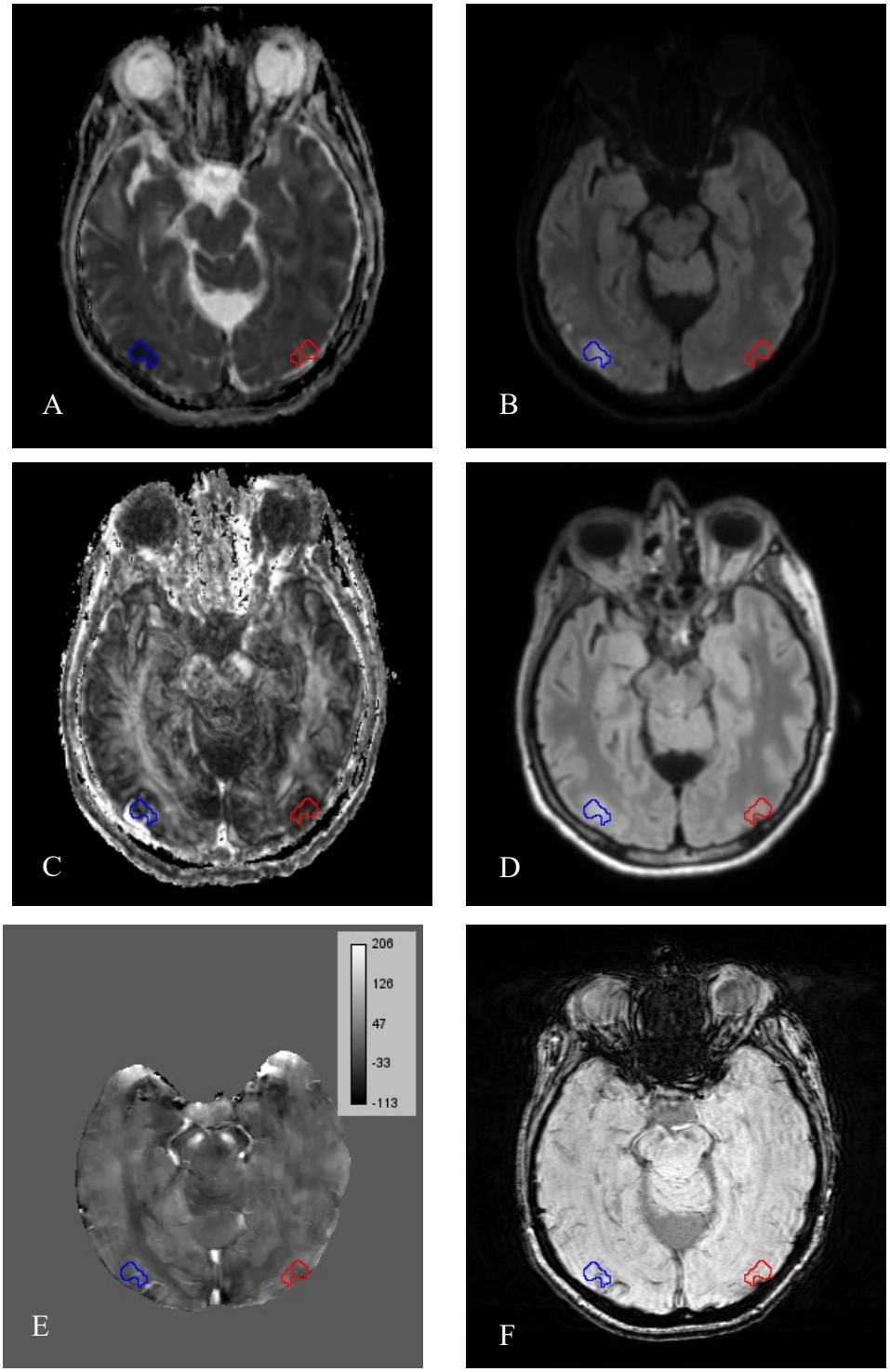

Figure 15 Grey matter tissue ROI on MD map (A), DWI (B), FA map (C), MPRAGE (D), QSM in ppb (E), SWI (F). Size of the lesion was 78.46 mm^2. Blue ROI is from infarcted region and red ROI is from the contralateral homologous region.

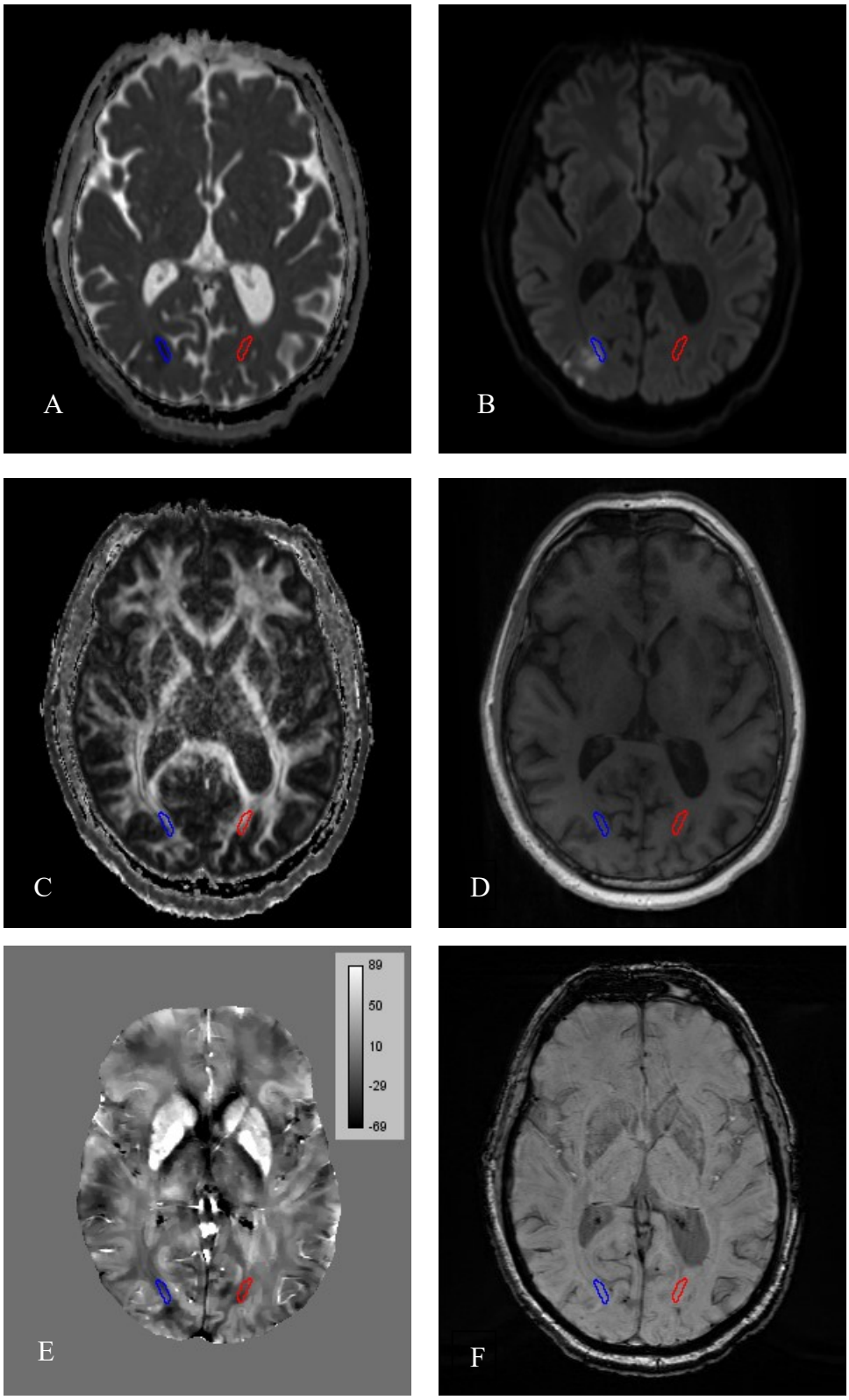

Figure 16 White matter tissue ROI on MD map (A), DWI (B), FA map (C), MPRAGE (D), QSM in ppb (E), SWI (F). Size of the lesion was 35.45 mm2. Blue ROI is from infarcted region and red ROI is from the contralateral homologous region.

Table 4 Mean susceptibility measurements of white matter (WM) tissue, grey matter (GM), major veins and local veins in stroke versus control hemisphere for subgroup A patients – mild stroke

Susceptibility Measure (ppb) †	Stroke Hemisphere	Control Hemisphere	*p* value
Major Vein Susceptibility	127.0[100.0,181.0]	90.0[66.0,107.0]	0.001*
Local Vein Susceptibility	80.0[66.2,85.5]	50.0[45.5,70.0]	0.0005*
Tissue Susceptibility (WM)	-6.0[-19.5,7.5]	-7.5[-26.5,-0.8]	0.0360*
Tissue Susceptibility (GM)	4.5[-5.7,37]	3.5[-15.7,35.7]	0.94

** p<0.05 significant, †Median [25%,75%]*

Table 5 Mean susceptibility measurements of white matter (WM) tissue, grey matter (GM), major veins and local veins in stroke versus control hemisphere for subgroup B patients – severe stroke

Susceptibility Measure (ppb) †	Stroke Hemisphere	Control Hemisphere	*p* value
Major Vein Susceptibility	125.5[105.5,170.3]	94.5[74.5,128.3]	0.0005*
Local Vein Susceptibility	78.5[60.5,96.5]	46.5[35.2,62.5]	0.002*
Tissue Susceptibility (WM)	-8.0[-15,5.2]	-12.0[-24.0, -1.0]	0.0002*
Tissue Susceptibility (GM)	9.0[-3.5,29]	1.0[-5.0,40.0]	0.1

** p<0.05 significant, † Median [25%, 75%]*

Cerebral Microbleeds

Figure 17 shows a slice of brain with microbleeds depicted on SWI images, phase, local field (to remove the effect of background field) and QSM. Figure 18 illustrates how microbleeds are depicted on SWI and QSM images.

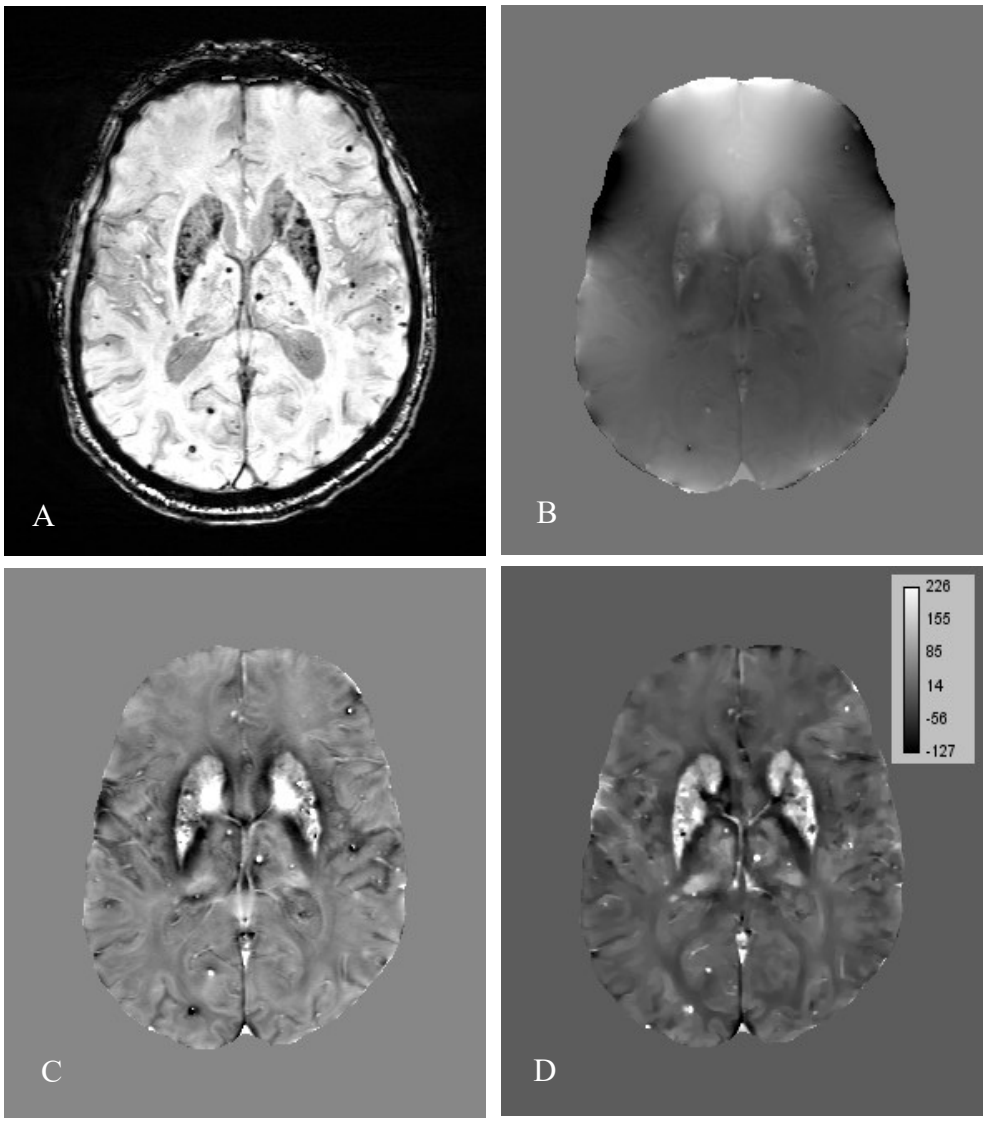

Figure 17 Microbleeds depicted on SWI (A), phase (B), local field (C) and QSM (D).

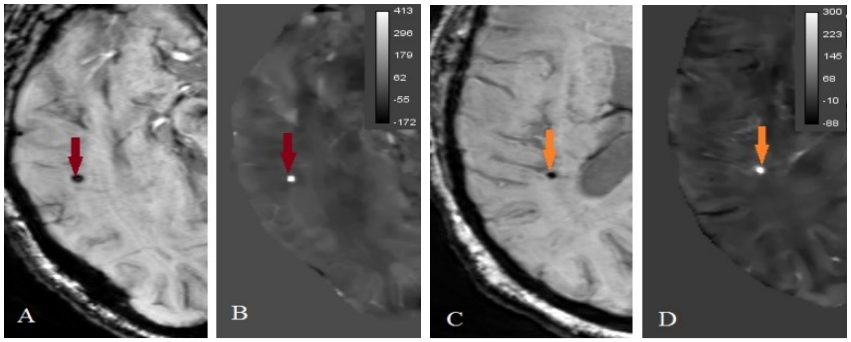

Figure 18 Microbleeds are depicted as hypointense on SWI (A, C) or hyperintense on QSM (B, D). Susceptibility in parts per billion (ppb).

Results from microbleeds assessment show a significant correlation between size and susceptibility of microbleed (r=0.3736, $p< 0.0001$) (Figure 19A). Correlation of microbleed susceptibility and ratio of area on SWI over QSM was assessed to evaluate the correlation of susceptibility value of the microbleed and blooming effect on SWI (Figure 19B) showing a significant correlation (r=0.5119, $p< 0.0001$) between the ratio of area on SWI compared to QSM and the susceptibility value. Based on the histogram and D'Agostino-Pearson omnibus normality test, all size and susceptibility measurements were non-normal and specific statistical methods were used. The size of microbleeds on SWI, QSM and magnitude images demonstrated that CMBs on QSM were significantly smaller than SW ($p< 0.0001$) and magnitude images ($p< 0.0001$) (Figure 19C). Wilcoxon matched-pairs signed rank test reported the magnetic susceptibility of microbleeds as 228.5[174, 330.8] ppb and the microbleed area on QSM as 2.42[1.84, 3.07] mm^2.

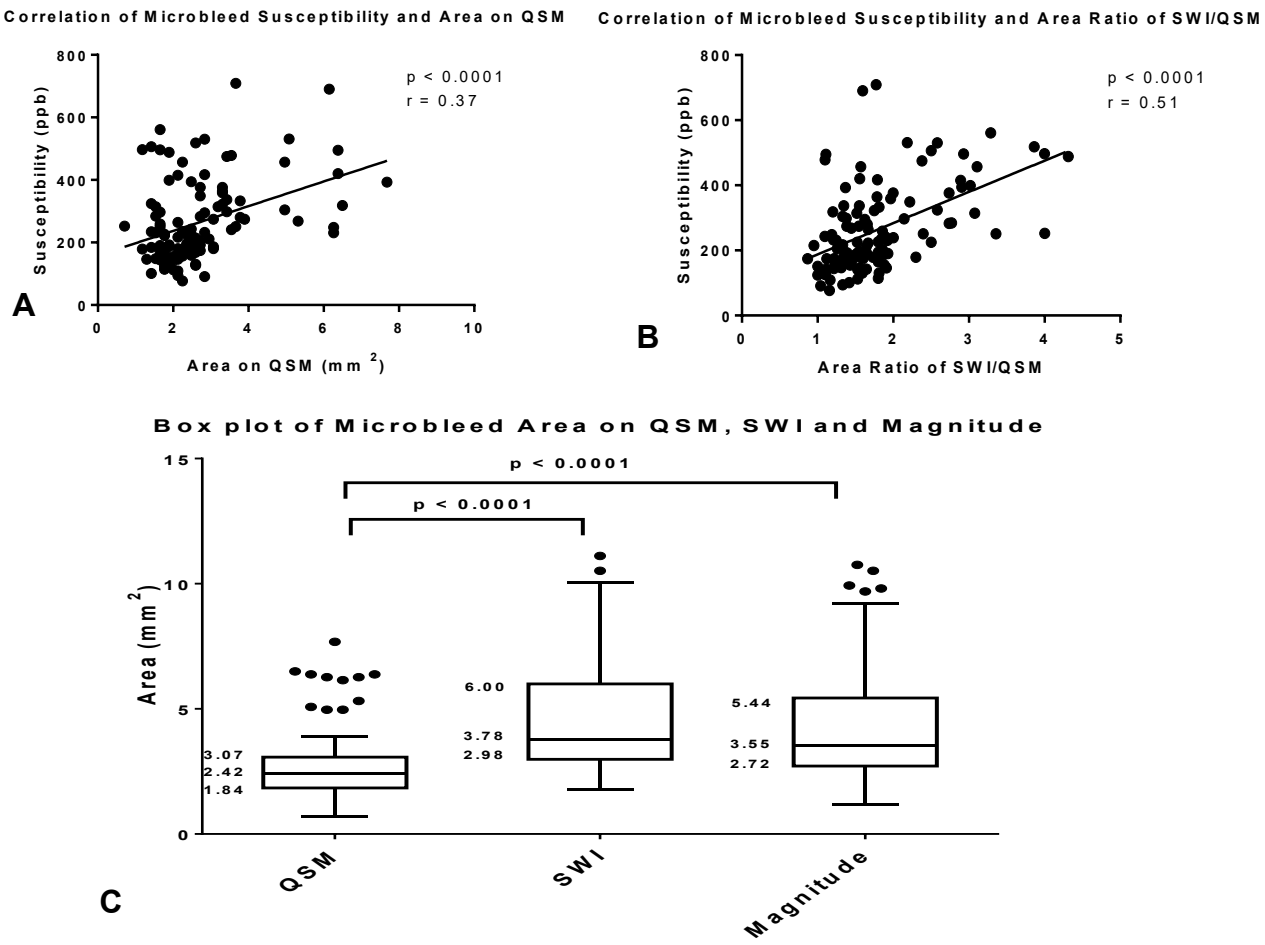

Figure 19 Findings of analyses of 116 detected microbleeds. Significant correlation of microbleed susceptibility and size on QSM images (A), significant correlation of microbleed susceptibility and size ratio on SWI to QSM (B), box plot of microbleed size distribution on QSM, SWI and magnitude images (C)

3.5. Discussion

We have demonstrated the use of QSM for three distinct measures in ischemic stroke: infarct and vein deoxygenation, and microbleed assessment. These QSM measurements required no additional MRI sequences and were performed by saving the raw phase images from standard SWI.

We found that QSM had significantly greater susceptibility for vein measurements in the infarcted hemisphere compared to the contralateral hemisphere and provided distinct definition of cerebral microbleeds. The increased vein susceptibility indicates higher blood deoxygenation in veins draining from lesion territory than that from contralateral side. The

elevated deoxyhemoglobin levels in draining veins from the infarct suggests a compromised arterial blood flow in the ischemic tissue. This result coincides with previous studies assessing MCA / carotid artery occlusion (66), and transient MCA occlusion in mouse brain (116).

Results from QSM tissue measurements were less clear. We observed a significant difference in white matter susceptibility assessment using QSM, while this difference was not observed in grey matter among patients in either of the subgroups. Factors such as lower collateral circulation (121), aging (122) and cellular type (123, 124) may make white matter more vulnerable to ischemic stroke than grey matter and could explain different sensitivity to ischemia.

Cerebral microbleed size on QSM was significantly smaller compared to SWI and magnitude. Both SW and magnitude images from SWI are susceptible to blooming artifact (105), which overestimates the lesion size. Although higher spatial resolution may be required for QSM to attain precise dimensions, it provides three key advantages over SWI. First, QSM may enable better quantification of microbleed size (95, 96), by removing the blooming signal artifacts originating from strong dipole field effects seen on SWI. The second advantage of QSM over SWI is detectability of microbleeds located in areas that are susceptible to air-tissue artifact where QSM can resolve this artifact and also enable separation of air from microbleed which are both hypointense on SWI. Finally, the measurement of QSM may eventually provide measures of tissue iron content and enable more effective segmentation of microbleeds by using thresholding on QSM. The range of susceptibility of microbleeds, 228.5[174.0, 330.8] ppb, compared to deep veins 108±56 ppb (95) suggest QSM as a potential semi-automated segmentation tool for microbleeds. Recent proposed automated methods have used SW imaging (125-127), and may benefit from QSM inclusion.

Limitations and future directions

Particularly for microbleeds, our data was limited by the spatial resolution in the slice dimension of only 2 mm. Higher spatial resolution would have allowed more precision in microbleed size and shape measures. Although QSM minimizes the blooming artifact seen on SWI and enables the assessment of microbleeds in regions with air-tissue artifact, the

QSM algorithm for background removal did not enable assessment of the 3 mm of tissue at brain edge. Using QSM reconstruction algorithms that enable whole brain maps might address this limitation (128, 129).

Another limitation is the small sample size that limits the power of the findings and the heterogeneity of the patient groups. Infarcts with different sizes and locations were considered and ROIs were separated into grey and white matter, limiting total measures for each category. Nevertheless, this study was able to show differences between infarcted and healthy regions and demonstrated that QSM delivers added value in stroke assessment.

A further limitation is the onset of cerebral microbleeds was unknown although a previous study suggests that there is no relationship between time after injury in transient ischemic attack patients and hemorrhage susceptibility (95). Future studies could include perfusion measures to locate the penumbra and assess the susceptibility difference between core and penumbra. Also, longitudinal studies could be performed to assess ischemic stroke evolution of tissue and vein susceptibility measurements.

3.6. Summary

Cerebral QSM in ischemic stroke patients provides valuable information on microbleed content, producing a quantitative measure with distinction between iron, air and calcium and removing blooming artifacts for more precise size measurements. Cerebral QSM also measures oxygenation differences in acute stroke, finding higher deoxygenation of the tissue infarct and draining veins compared to the contralateral side. Any study already utilizing SWI can perform QSM by saving the raw phase images, no additional MRI scan is required. Given its unique measures and lack of additional MRI cost, QSM is a valuable addition to any stroke study already incorporating SWI.

4. Conclusion

4.1. Summary of Findings

The main goals for this thesis were to examine the potential of QSM in providing information for three distinct measures among ischemic stroke patients: infarct and tissue deoxygenation in veins, and microbleed assessment.

A key finding of QSM in the acute stroke group was the significantly greater susceptibility for vein measurements in the infarcted hemisphere compared to the contralateral homologous hemisphere. The increased vein susceptibility is an indicator of higher blood deoxygenation in veins draining from the infarcted hemisphere than from the contralateral side. The elevated deoxyhemoglobin levels in draining veins from the infarct suggests a compromised arterial blood flow and collateral vascular distribution in the ischemic region. The result is in agreement with studies that assessed MCA / carotid artery occlusion (66), and transient MCA occlusion in mouse brain using QSM (116).

Also, a significant difference was observed in white matter susceptibility assessment using QSM. This difference that was observed as higher susceptibility of white matter in infarcted region compared to contralateral region, was not observed in grey matter. The relatively higher sensitivity of white matter to ischemia compared to grey matter can be due to factors such as lower collateral circulation (121), aging (122) and cellular type (123, 124).

Microbleed assessment using QSM showed three key advantages of QSM over the standard approach of SWI. First, better quantification of microbleed size and shape (95, 96) as well as quantitative measurement of susceptibility rather than the qualitative nature of SWI, enabling measurements of iron content. It also removes blooming signal artifacts originating from strong dipole field effects seen on SWI, enabling local measurements. Second, improved detectability of microbleeds located in areas that are susceptible to air-tissue artifact where QSM can resolve this artifact and also enable separation of air from microbleed which are both hypointense on SWI values. Finally, QSM may enable more effective segmentation of microbleeds by using thresholding on QSM combined vessel

continuity to exclude veins. The range of quantified susceptibility of microbleeds, 228.5[174.0, 330.8] ppb, compared to deep veins 108±56 ppb (95) suggest QSM as a potential semi-automated segmentation tool for microbleeds.

The value of QSM is further enhanced since QSM postprocessing can be performed on SWI images and does not require additional MRI sequences.

4.2. Limitations

One of the factors that limited the power of the findings regarding vein and tissue oxygenation assessment in this study was the heterogeneity of the patient groups and relatively small sample size. Also, different sizes and locations of the infarcts limited the number of ROIs in white and grey matter. Nevertheless, this study was able to show differences between infarcted and healthy regions and demonstrated that QSM delivers added value in stroke assessment.

Particularly for microbleeds, our data was limited by the spatial resolution in the slice dimension of only 2 mm. Higher spatial resolution would have allowed more precision in microbleed size and shape measures.

The QSM method also has an inherent limitation of not being that sensitive to small changes in oxygenation. For example, in functional brain mapping studies, it has been found that magnitude changes in blood oxygenation levels are more sensitive and robust to cerebral flow/ oxygenation studies than QSM (130). QSM may lack the sensitivity to be used in small strokes.

A further limitation of the QSM method was the background removal algorithm. Although QSM enables the assessment of microbleeds in regions with air-tissue artifact, the background removal algorithm does not assess 3 mm of tissue at brain edges. By using QSM reconstructions that provide the whole brain map without skull stripping (128, 129), this limitation can be addressed. However, the new whole brain QSM methods are not fully proven at this time.

4.3. Future Directions

There are still areas of improvement in QSM development. The reconstruction of QSM from phase images is a relatively time-consuming process and is performed off-line. In the future, QSM reconstruction can be done on scanner console and susceptibility maps would be computed real time(131). Methods to reconstruct the whole brain with QSM (128) could also be explored to capture the outer cortex region that is currently lost. Better methods to deal with patient motion are also needed, since this motion can strongly affect phase images (132).

The potential and value of QSM in other pathologies can be assessed in the future. Particularly in stroke, future studies could include perfusion measures to locate the penumbra and assess the susceptibility difference between core and penumbra. Also, longitudinal studies could be performed to assess ischemic stroke evolution of tissue and vein susceptibility measurements. Furthermore, by studying larger number of cases, the possible correlation of age, gender, ethnicity and other measures with stroke outcomes and susceptibility measurements can be evaluated.

In conclusion, QSM methods in stroke are still in their infancy and more research is needed in both fundamental QSM methods and clinical studies.

Bibliography

1. Liang Z-P, Lauterbur PC. Principles of magnetic resonance imaging: a signal processing perspective: SPIE Optical Engineering Press; 2000.
2. Brown RW, Haacke EM, Cheng Y-CN, Thompson MR, Venkatesan R. Magnetic resonance imaging: physical principles and sequence design: John Wiley & Sons; 2014.
3. Bernstein MA, King KF, Zhou XJ. Handbook of MRI pulse sequences: Elsevier; 2004.
4. He X, Yablonskiy DAJPotNAoS. Biophysical mechanisms of phase contrast in gradient echo MRI. 2009;106(32):13558-63.
5. Rauscher A, Sedlacik J, Barth M, Mentzel H-J, Reichenbach JRJAjon. Magnetic susceptibility-weighted MR phase imaging of the human brain. 2005;26(4):736-42.
6. Duyn JH, van Gelderen P, Li T-Q, de Zwart JA, Koretsky AP, Fukunaga MJPotNAoS. High-field MRI of brain cortical substructure based on signal phase. 2007;104(28):11796-801.
7. Gatehouse PD, Keegan J, Crowe LA, Masood S, Mohiaddin RH, Kreitner K-F, et al. Applications of phase-contrast flow and velocity imaging in cardiovascular MRI. 2005;15(10):2172-84.
8. Lee J, Shmueli K, Fukunaga M, van Gelderen P, Merkle H, Silva AC, et al. Sensitivity of MRI resonance frequency to the orientation of brain tissue microstructure. Proceedings of the National Academy of Sciences. 2010:200910222.
9. Shmueli K, de Zwart JA, van Gelderen P, Li TQ, Dodd SJ, Duyn JH. Magnetic susceptibility mapping of brain tissue in vivo using MRI phase data. Magnetic Resonance in Medicine: An Official Journal of the International Society for Magnetic Resonance in Medicine. 2009;62(6):1510-22.
10. Haacke EM, Reichenbach JR. Susceptibility weighted imaging in MRI: basic concepts and clinical applications: John Wiley & Sons; 2014.
11. Formica D, Silvestri SJBeo. Biological effects of exposure to magnetic resonance imaging: an overview. 2004;3(1):11.
12. Haacke EM, Xu Y, Cheng YCN, Reichenbach JR. Susceptibility weighted imaging (SWI). Magnetic Resonance in Medicine: An Official Journal of the International Society for Magnetic Resonance in Medicine. 2004;52(3):612-8.
13. Haacke EM, Mittal S, Wu Z, Neelavalli J, Cheng Y-C. Susceptibility-weighted imaging: technical aspects and clinical applications, part 1. American Journal of Neuroradiology. 2009;30(1):19-30.
14. Mittal S, Wu Z, Neelavalli J, Haacke EM. Susceptibility-weighted imaging: technical aspects and clinical applications, part 2. American Journal of neuroradiology. 2009;30(2):232-52.
15. Liu C, Li W, Tong KA, Yeom KW, Kuzminski S. Susceptibility-weighted imaging and quantitative susceptibility mapping in the brain. Journal of magnetic resonance imaging. 2015;42(1):23-41.
16. de Rochefort L, Liu T, Kressler B, Liu J, Spincemaille P, Lebon V, et al. Quantitative susceptibility map reconstruction from MR phase data using bayesian regularization: validation and application to brain imaging. Magnetic resonance in medicine. 2010;63(1):194-206.
17. Schweser F, Deistung A, Lehr BW, Reichenbach JR. Differentiation between diamagnetic and paramagnetic cerebral lesions based on magnetic susceptibility mapping. Medical physics. 2010;37(10):5165-78.
18. Schäfer A, Gowland PA, Bowtell RW, editors. Using field simulations to understand susceptibility related phase contrast in high field gradient echo images. Proc Intl Soc Mag Reson Med; 2008.

19. Haacke EM, Liu S, Buch S, Zheng W, Wu D, Ye Y. Quantitative susceptibility mapping: current status and future directions. Magnetic resonance imaging. 2015;33(1):1-25.
20. Schäfer A, Wharton S, Gowland P, Bowtell R. Using magnetic field simulation to study susceptibility-related phase contrast in gradient echo MRI. Neuroimage. 2009;48(1):126-37.
21. Salomir R, de Senneville BD, Moonen CT. A fast calculation method for magnetic field inhomogeneity due to an arbitrary distribution of bulk susceptibility. Concepts in Magnetic Resonance Part B: Magnetic Resonance Engineering: An Educational Journal. 2003;19(1):26-34.
22. Wang Y, Liu T. Quantitative susceptibility mapping (QSM): decoding MRI data for a tissue magnetic biomarker. Magnetic resonance in medicine. 2015;73(1):82-101.
23. Jenkinson M. Fast, automated, N-dimensional phase-unwrapping algorithm. Magnetic Resonance in Medicine: An Official Journal of the International Society for Magnetic Resonance in Medicine. 2003;49(1):193-7.
24. Neelavalli J, Cheng YCN, Jiang J, Haacke EM. Removing background phase variations in susceptibility-weighted imaging using a fast, forward-field calculation. Journal of Magnetic Resonance Imaging: An Official Journal of the International Society for Magnetic Resonance in Medicine. 2009;29(4):937-48.
25. Smith SM. Fast robust automated brain extraction. Human brain mapping. 2002;17(3):143-55.
26. Wang Y, Yu Y, Li D, Bae K, Brown J, Lin W, et al. Artery and vein separation using susceptibility-dependent phase in contrast-enhanced MRA. Journal of Magnetic Resonance Imaging. 2000;12(5):661-70.
27. Langham MC, Magland JF, Floyd TF, Wehrli FW. Retrospective correction for induced magnetic field inhomogeneity in measurements of large-vessel hemoglobin oxygen saturation by MR susceptometry. Magnetic Resonance in Medicine: An Official Journal of the International Society for Magnetic Resonance in Medicine. 2009;61(3):626-33.
28. Liu T, Khalidov I, de Rochefort L, Spincemaille P, Liu J, Tsiouris AJ, et al. A novel background field removal method for MRI using projection onto dipole fields. NMR in Biomedicine. 2011;24(9):1129-36.
29. Schweser F, Deistung A, Lehr BW, Reichenbach JR. Quantitative imaging of intrinsic magnetic tissue properties using MRI signal phase: an approach to in vivo brain iron metabolism? Neuroimage. 2011;54(4):2789-807.
30. Schweser F, Robinson SD, de Rochefort L, Li W, Bredies K. An illustrated comparison of processing methods for phase MRI and QSM: removal of background field contributions from sources outside the region of interest. NMR in Biomedicine. 2017;30(4):e3604.
31. Sun H, Wilman AH. Background field removal using spherical mean value filtering and Tikhonov regularization. Magnetic resonance in medicine. 2014;71(3):1151-7.
32. Liu T, Spincemaille P, De Rochefort L, Kressler B, Wang Y. Calculation of susceptibility through multiple orientation sampling (COSMOS): a method for conditioning the inverse problem from measured magnetic field map to susceptibility source image in MRI. Magnetic Resonance in Medicine: An Official Journal of the International Society for Magnetic Resonance in Medicine. 2009;61(1):196-204.
33. Haacke E, Tang J, Neelavalli J, Cheng Y. Susceptibility mapping as a means to visualize veins and quantify oxygen saturation. Journal of Magnetic Resonance Imaging. 2010;32(3):663-76.
34. Kressler B, De Rochefort L, Liu T, Spincemaille P, Jiang Q, Wang Y. Nonlinear regularization for per voxel estimation of magnetic susceptibility distributions from MRI field maps. IEEE transactions on medical imaging. 2010;29(2):273-81.
35. Bilgic B, Pfefferbaum A, Rohlfing T, Sullivan EV, Adalsteinsson E. MRI estimates of brain iron concentration in normal aging using quantitative susceptibility mapping. Neuroimage. 2012;59(3):2625-35.

36. Bilgic B, Fan AP, Polimeni JR, Cauley SF, Bianciardi M, Adalsteinsson E, et al. Fast quantitative susceptibility mapping with L1-regularization and automatic parameter selection. Magnetic resonance in medicine. 2014;72(5):1444-59.
37. Lustig M, Donoho D, Pauly JM. Sparse MRI: The application of compressed sensing for rapid MR imaging. Magnetic Resonance in Medicine: An Official Journal of the International Society for Magnetic Resonance in Medicine. 2007;58(6):1182-95.
38. Klohs J, Deistung A, Schweser F, Grandjean J, Dominietto M, Waschkies C, et al. Detection of cerebral microbleeds with quantitative susceptibility mapping in the ArcAbeta mouse model of cerebral amyloidosis. Journal of Cerebral Blood Flow Metabolism. 2011;31(12):2282-92.
39. Deistung A, Schweser F, Wiestler B, Abello M, Roethke M, Sahm F, et al. Quantitative susceptibility mapping differentiates between blood depositions and calcifications in patients with glioblastoma. PloS one. 2013;8(3):e57924.
40. Langkammer C, Liu T, Khalil M, Enzinger C, Jehna M, Fuchs S, et al. Quantitative susceptibility mapping in multiple sclerosis. Radiology. 2013;267(2):551-9.
41. Rudko DA, Solovey I, Gati JS, Kremenchutzky M, Menon RS. Multiple sclerosis: improved identification of disease-relevant changes in gray and white matter by using susceptibility-based MR imaging. Radiology. 2014;272(3):851-64.
42. Xia S, Utriainen D, Tang J, Kou Z, Zheng G, Wang X, et al. Decreased oxygen saturation in asymmetrically prominent cortical veins in patients with cerebral ischemic stroke. Magnetic resonance imaging. 2014;32(10):1272-6.
43. Jensen-Kondering U, Böhm R. Asymmetrically hypointense veins on T2* w imaging and susceptibility-weighted imaging in ischemic stroke. World journal of radiology. 2013;5(4):156.
44. Eskreis-Winkler S, Zhang Y, Zhang J, Liu Z, Dimov A, Gupta A, et al. The clinical utility of QSM: disease diagnosis, medical management, and surgical planning. NMR in Biomedicine. 2017;30(4):e3668.
45. Liu C, Wei H, Gong N-J, Cronin M, Dibb R, Decker K. Quantitative susceptibility mapping: contrast mechanisms and clinical applications. Tomography: a journal for imaging research. 2015;1(1):3.
46. Deistung A, Schweser F, Reichenbach JR. Overview of quantitative susceptibility mapping. NMR in Biomedicine. 2017;30(4):e3569.
47. LeVine SM. Iron deposits in multiple sclerosis and Alzheimer's disease brains. Brain research. 1997;760(1-2):298-303.
48. Bouras C, Giannakopoulos P, Good PF, Hsu A, Hof PR, Perl DP. A laser microprobe mass analysis of brain aluminum and iron in dementia pugilistica: comparison with Alzheimer's disease. European neurology. 1997;38(1):53-8.
49. Dexter D, Carayon A, Javoy-Agid F, Agid Y, Wells F, Daniel S, et al. Alterations in the levels of iron, ferritin and other trace metals in Parkinson's disease and other neurodegenerative diseases affecting the basal ganglia. Brain. 1991;114(4):1953-75.
50. Chen JC, Hardy P, Kucharczyk W, Clauberg M, Joshi J, Vourlas A, et al. MR of human postmortem brain tissue: correlative study between T2 and assays of iron and ferritin in Parkinson and Huntington disease. American journal of neuroradiology. 1993;14(2):275-81.
51. Haraguchi T, Terada S, Ishizu H, Yokota O, Yoshida H, Takeda N, et al. Coexistence of TDP-43 and tau pathology in neurodegeneration with brain iron accumulation type 1 (NBIA-1, formerly Hallervorden-Spatz syndrome). Neuropathology. 2011;31(5):531-9.
52. Hallgren B, Sourander P. The effect of age on the non-haemin iron in the human brain. Journal of neurochemistry. 1958;3(1):41-51.
53. Barbosa JHO, Santos AC, Tumas V, Liu M, Zheng W, Haacke EM, et al. Quantifying brain iron deposition in patients with Parkinson's disease using quantitative susceptibility mapping, R2 and R2. Magnetic resonance imaging. 2015;33(5):559-65.

54. Du G, Liu T, Lewis MM, Kong L, Wang Y, Connor J, et al. Quantitative susceptibility mapping of the midbrain in Parkinson's disease. Movement Disorders. 2016;31(3):317-24.
55. Acosta-Cabronero J, Williams GB, Cardenas-Blanco A, Arnold RJ, Lupson V, Nestor PJ. In vivo quantitative susceptibility mapping (QSM) in Alzheimer's disease. PloS one. 2013;8(11):e81093.
56. Stüber C, Pitt D, Wang Y. Iron in multiple sclerosis and its noninvasive imaging with quantitative susceptibility mapping. International journal of molecular sciences. 2016;17(1):100.
57. Eskreis-Winkler S, Deh K, Gupta A, Liu T, Wisnieff C, Jin M, et al. Multiple sclerosis lesion geometry in quantitative susceptibility mapping (QSM) and phase imaging. Journal of Magnetic Resonance Imaging. 2015;42(1):224-9.
58. Chen W, Gauthier SA, Gupta A, Comunale J, Liu T, Wang S, et al. Quantitative susceptibility mapping of multiple sclerosis lesions at various ages. Radiology. 2014;271(1):183-92.
59. Guan X, Xuan M, Gu Q, Huang P, Liu C, Wang N, et al. Regionally progressive accumulation of iron in Parkinson's disease as measured by quantitative susceptibility mapping. NMR in Biomedicine. 2017;30(4):e3489.
60. Sun H, Klahr AC, Kate M, Gioia LC, Emery DJ, Butcher KS, et al. Quantitative Susceptibility Mapping for Following Intracranial Hemorrhage. Radiology. 2018:171918.
61. Fan AP, Bilgic B, Gagnon L, Witzel T, Bhat H, Rosen BR, et al. Quantitative oxygenation venography from MRI phase. Magnetic resonance in medicine. 2014;72(1):149-59.
62. Fan AP, Benner T, Bolar DS, Rosen BR, Adalsteinsson E. Phase-based regional oxygen metabolism (PROM) using MRI. Magnetic resonance in medicine. 2012;67(3):669-78.
63. Xu B, Liu T, Spincemaille P, Prince M, Wang Y. Flow compensated quantitative susceptibility mapping for venous oxygenation imaging. Magnetic resonance in medicine. 2014;72(2):438-45.
64. Yadav BK, Buch S, Krishnamurthy U, Jella P, Hernandez-Andrade E, Trifan A, et al. Quantitative susceptibility mapping in the human fetus to measure blood oxygenation in the superior sagittal sinus. European radiology. 2018:1-10.
65. Kudo K, Liu T, Murakami T, Goodwin J, Uwano I, Yamashita F, et al. Oxygen extraction fraction measurement using quantitative susceptibility mapping: comparison with positron emission tomography. Journal of Cerebral Blood Flow Metabolism. 2016;36(8):1424-33.
66. Uwano I, Kudo K, Sato R, Ogasawara K, Kameda H, Nomura J-i, et al. Noninvasive assessment of oxygen extraction fraction in chronic ischemia using quantitative susceptibility mapping at 7 Tesla. Stroke. 2017;48(8):2136-41.
67. Hankey GJJTLGH. The global and regional burden of stroke. 2013;1(5):e239-e40.
68. Davis SM, Donnan GAJNEJoM. Secondary prevention after ischemic stroke or transient ischemic attack. 2012;366(20):1914-22.
69. Amarenco P, Cohen A, Tzourio C, Bertrand B, Hommel M, Besson G, et al. Atherosclerotic disease of the aortic arch and the risk of ischemic stroke. New England Journal of Medicine. 1994;331(22):1474-9.
70. Petty GW, Brown Jr RD, Whisnant JP, Sicks JD, O'Fallon WM, Wiebers DO. Ischemic stroke subtypes: a population-based study of incidence and risk factors. Stroke. 1999;30(12):2513-6.
71. Ross R. Atherosclerosis—an inflammatory disease. New England journal of medicine. 1999;340(2):115-26.
72. Balami JS, Buchan AM. Complications of intracerebral haemorrhage. The Lancet Neurology. 2012;11(1):101-18.
73. van Asch CJ, Luitse MJ, Rinkel GJ, van der Tweel I, Algra A, Klijn CJ. Incidence, case fatality, and functional outcome of intracerebral haemorrhage over time, according to age, sex, and ethnic origin: a systematic review and meta-analysis. The Lancet Neurology. 2010;9(2):167-76.

74. Barnes B, Hanley DF, Carhuapoma JR. Minimally invasive surgery for intracerebral haemorrhage. Current opinion in critical care. 2014;20(2):148.
75. Hanley DF, Awad IA, Vespa PM, Martin NA, Zuccarello M. Hemorrhagic stroke: introduction. Stroke. 2013;44(6 suppl 1):S65-S6.
76. Suarez JI, Tarr RW, Selman WR. Aneurysmal subarachnoid hemorrhage. New England Journal of Medicine. 2006;354(4):387-96.
77. Rinkel G. Subarachnoid haemorrhage: diagnosis, causes and management. Brain: a journal of neurology. 2001;124(Pt 2):249-78.
78. Kidwell CS, Villablanca JP, Saver JL. Advances in neuroimaging of acute stroke. urrent atherosclerosis reports. 2000;2(2):126-35.
79. Jauch EC, Saver JL, Adams Jr HP, Bruno A, Connors J, Demaerschalk BM, et al. Guidelines for the early management of patients with acute ischemic stroke: a guideline for healthcare professionals from the American Heart Association/American Stroke Association. 2013;44(3):870-947.
80. Kidwell CS, Alger JR, Di Salle F, Starkman S, Villablanca P, Bentson J, et al. Diffusion MRI in patients with transient ischemic attacks. Stroke. 1999;30(6):1174-80.
81. Patel SC, Levine SR, Tilley BC, Grotta JC, Lu M, Frankel M, et al. Lack of clinical significance of early ischemic changes on computed tomography in acute stroke. Jama. 2001;286(22):2830-8.
82. Chalela JA, Kidwell CS, Nentwich LM, Luby M, Butman JA, Demchuk AM, et al. Magnetic resonance imaging and computed tomography in emergency assessment of patients with suspected acute stroke: a prospective comparison. The Lancet. 2007;369(9558):293-8.
83. Bash S, Villablanca JP, Jahan R, Duckwiler G, Tillis M, Kidwell C, et al. Intracranial vascular stenosis and occlusive disease: evaluation with CT angiography, MR angiography, and digital subtraction angiography. American Journal of Neuroradiology. 2005;26(5):1012-21.
84. Fiebach J, Schellinger P, Jansen O, Meyer M, Wilde P, Bender J, et al. CT and diffusion-weighted MR imaging in randomized order: diffusion-weighted imaging results in higher accuracy and lower interrater variability in the diagnosis of hyperacute ischemic stroke. Stroke. 2002;33(9):2206-10.
85. Gonzalez RG, Schaefer PW, Buonanno FS, Schwamm LH, Budzik RF, Rordorf G, et al. Diffusion-weighted MR imaging: diagnostic accuracy in patients imaged within 6 hours of stroke symptom onset. Radiology. 1999;210(1):155-62.
86. Fisher M, Albers GW. Applications of diffusion–perfusion magnetic resonance imaging in acute ischemic stroke. Neurology. 1999;52(9):1750-.
87. Parsons MW, Barber PA, Chalk J, Darby DG, Rose S, Desmond PM, et al. Diffusion-and perfusion-weighted MRI response to thrombolysis in stroke. Annals of Neurology: Official Journal of the American Neurological Association

the Child Neurology Society. 2002;51(1):28-37.
88. Löuvbld KO, Baird AE, Schlaug G, Benfield A, Siewert B, Voetsch B, et al. Ischemic lesion volumes in acute stroke by diffusion-weighted magnetic resonance imaging correlate with clinical outcome. Annals of Neurology: Official Journal of the American Neurological Association

the Child Neurology Society. 1997;42(2):164-70.
89. Beaulieu C, De Crespigny A, Tong DC, Moseley ME, Albers GW, Marks MP. Longitudinal magnetic resonance imaging study of perfusion and diffusion in stroke: evolution of lesion volume and correlation with clinical outcome. Annals of Neurology: Official Journal of the American Neurological Association

the Child Neurology Society. 1999;46(4):568-78.
90. Lansberg MG, Albers GW, Beaulieu C, Marks MP. Comparison of diffusion-weighted MRI and CT in acute stroke. Neurology. 2000;54(8):1557-61.

91. Warach S, Li W, Ronthal M, Edelman RR. Acute cerebral ischemia: evaluation with dynamic contrast-enhanced MR imaging and MR angiography. Radiology. 1992;182(1):41-7.
92. Meoded A, Poretti A, Benson JE, Tekes A, Huisman TA. Evaluation of the ischemic penumbra focusing on the venous drainage: the role of susceptibility weighted imaging (SWI) in pediatric ischemic cerebral stroke. Journal of Neuroradiology. 2014;41(2):108-16.
93. Chen C-Y, Chen C-I, Tsai FY, Tsai P-H, Chan WPJPo. Prominent vessel sign on susceptibility-weighted imaging in acute stroke: prediction of infarct growth and clinical outcome. 2015;10(6):e0131118.
94. Liu S, Buch S, Chen Y, Choi HS, Dai Y, Habib C, et al. Susceptibility-weighted imaging: current status and future directions. NMR in Biomedicine. 2017;30(4):e3552.
95. Liu J, Xia S, Hanks R, Wiseman N, Peng C, Zhou S, et al. Susceptibility weighted imaging and mapping of micro-hemorrhages and major deep veins after traumatic brain injury. Journal of neurotrauma. 2016;33(1):10-21.
96. Greenberg SM, Vernooij MW, Cordonnier C, Viswanathan A, Salman RA-S, Warach S, et al. Cerebral microbleeds: a guide to detection and interpretation. The Lancet Neurology. 2009;8(2):165-74.
97. Fan YH, Zhang L, Lam WW, Mok VC, Wong KS. Cerebral microbleeds as a risk factor for subsequent intracerebral hemorrhages among patients with acute ischemic stroke. Stroke. 2003;34(10):2459-62.
98. Lee S, Bae H, Kwon S, Kim H, Kim Y, Yoon B, et al. Cerebral microbleeds are regionally associated with intracerebral hemorrhage. Neurology. 2004;62(1):72-6.
99. Nighoghossian N, Hermier M, Adeleine P, Blanc-Lasserre K, Derex L, Honnorat J, et al. Old microbleeds are a potential risk factor for cerebral bleeding after ischemic stroke: a gradient-echo T2*-weighted brain MRI study. Stroke. 2002;33(3):735-42.
100. Jeerakathil T, Wolf PA, Beiser A, Hald JK, Au R, Kase CS, et al. Cerebral microbleeds: prevalence and associations with cardiovascular risk factors in the Framingham Study. Stroke. 2004;35(8):1831-5.
101. Benedictus MR, Goos JD, Binnewijzend MA, Muller M, Barkhof F, Scheltens P, et al. Specific risk factors for microbleeds and white matter hyperintensities in Alzheimer's disease. Neurobiology of aging. 2013;34(11):2488-94.
102. Ayaz M, Boikov AS, Haacke EM, Kido DK, Kirsch WM. Imaging cerebral microbleeds using susceptibility weighted imaging: one step toward detecting vascular dementia. Journal of Magnetic Resonance Imaging. 2010;31(1):142-8.
103. Won Seo S, Hwa Lee B, Kim E-J, Chin J, Sun Cho Y, Yoon U, et al. Clinical significance of microbleeds in subcortical vascular dementia. Stroke. 2007;38(6):1949-51.
104. Park J-H, Park S-W, Kang S-H, Nam T-K, Min B-K, Hwang S-N. Detection of traumatic cerebral microbleeds by susceptibility-weighted image of MRI. Journal of Korean Neurosurgical Society. 2009;46(4):365.
105. Buch S, Cheng YCN, Hu J, Liu S, Beaver J, Rajagovindan R, et al. Determination of detection sensitivity for cerebral microbleeds using susceptibility-weighted imaging. NMR in biomedicine. 2017;30(4):e3551.
106. Cordonnier C, Al-Shahi Salman R, Wardlaw J. Spontaneous brain microbleeds: systematic review, subgroup analyses and standards for study design and reporting. Brain. 2007;130(8):1988-2003.
107. Conijn MM, Geerlings MI, Luijten PR, Zwanenburg JJ, Visser F, Biessels GJ, et al. Visualization of cerebral microbleeds with dual-echo T2*-weighted magnetic resonance imaging at 7.0 T. Journal of Magnetic Resonance Imaging. 2010;32(1):52-9.
108. Gass A, Ay H, Szabo K, Koroshetz WJ. Diffusion-weighted MRI for the “small stuff”: the details of acute cerebral ischaemia. The Lancet Neurology. 2004;3(1):39-45.

109. Vymazal J, Rulseh AM, Keller J, Janouskova LJIii. Comparison of CT and MR imaging in ischemic stroke. 2012;3(6):619-27.
110. Lin MP, Liebeskind DS. Imaging of ischemic stroke. Continuum: Lifelong Learning in Neurology. 2016;22(5):1399.
111. Wycliffe ND, Choe J, Holshouser B, Oyoyo UE, Haacke EM, Kido DK. Reliability in detection of hemorrhage in acute stroke by a new three-dimensional gradient recalled echo susceptibility-weighted imaging technique compared to computed tomography: a retrospective study. Journal of Magnetic Resonance Imaging: An Official Journal of the International Society for Magnetic Resonance in Medicine. 2004;20(3):372-7.
112. Wilson D, Ambler G, Shakeshaft C, Brown MM, Charidimou A, Salman RA-S, et al. Cerebral microbleeds and intracranial haemorrhage risk in patients anticoagulated for atrial fibrillation after acute ischaemic stroke or transient ischaemic attack (CROMIS-2): a multicentre observational cohort study. The Lancet Neurology. 2018;17(6):539-47.
113. Li J, Chang S, Liu T, Wang Q, Cui D, Chen X, et al. Reducing the object orientation dependence of susceptibility effects in gradient echo MRI through quantitative susceptibility mapping. Magnetic resonance in medicine. 2012;68(5):1563-9.
114. Neubauer R, James P. Cerebral oxygenation and the recoverable brain. Neurological research. 1998;20(sup1):S33-S6.
115. Luo Y, Gong Z, Zhou Y, Chang B, Chai C, Liu T, et al. Increased susceptibility of asymmetrically prominent cortical veins correlates with misery perfusion in patients with occlusion of the middle cerebral artery. European radiology. 2017;27(6):2381-90.
116. Vaas M, Deistung A, Reichenbach JR, Keller A, Kipar A, Klohs J. Vascular and tissue changes of magnetic susceptibility in the mouse brain after transient cerebral ischemia. Translational stroke research. 2018;9(4):426-35.
117. Bivard A, Lou M, Levi CR, Krishnamurthy V, Cheng X, Aviv RI, et al. Too good to treat? ischemic stroke patients with small computed tomography perfusion lesions may not benefit from thrombolysis. Annals of neurology. 2016;80(2):286-93.
118. Jenkinson M, Bannister P, Brady M, Smith S. Improved optimization for the robust and accurate linear registration and motion correction of brain images. Neuroimage. 2002;17(2):825-41.
119. Mugler III JP, Brookeman JR. Three-dimensional magnetization-prepared rapid gradient-echo imaging (3D MP RAGE). Magnetic Resonance in Medicine. 1990;15(1):152-7.
120. Haller S, Vernooij MW, Kuijer JP, Larsson E-M, Jäger HR, Barkhof F. Cerebral Microbleeds: Imaging and Clinical Significance. Radiology. 2018;287(1):11-28.
121. Wang Y, Liu G, Hong D, Chen F, Ji X, Cao G. White matter injury in ischemic stroke. Progress in neurobiology. 2016;141:45-60.
122. Correa F, Gauberti M, Parcq J, Macrez R, Hommet Y, Obiang P, et al. Tissue plasminogen activator prevents white matter damage following stroke. Journal of Experimental Medicine. 2011;208(6):1229-42.
123. Husain J, Juurlink BH. Oligodendroglial precursor cell susceptibility to hypoxia is related to poor ability to cope with reactive oxygen species. Brain research. 1995;698(1-2):86-94.
124. Káradóttir R, Cavelier P, Bergersen LH, Attwell D. NMDA receptors are expressed in oligodendrocytes and activated in ischaemia. Nature. 2005;438(7071):1162.
125. van den Heuvel T, van der Eerden A, Manniesing R, Ghafoorian M, Tan T, Andriessen T, et al. Automated detection of cerebral microbleeds in patients with traumatic brain injury. NeuroImage: Clinical. 2016;12:241-51.

126. Standvoss K, Crijns T, Goerke L, Janssen D, Kern S, van Niedek T, et al., editors. Cerebral microbleed detection in traumatic brain injury patients using 3D convolutional neural networks. Medical Imaging 2018: Computer-Aided Diagnosis; 2018: International Society for Optics and Photonics.
127. Wang S, Jiang Y, Hou X, Cheng H, Du S. Cerebral micro-bleed detection based on the convolution neural network with rank based average pooling. IEEE Access. 2017;5:16576-83.
128. Sun H, Ma Y, MacDonald ME, Pike GB. Whole head quantitative susceptibility mapping using a least-norm direct dipole inversion method. NeuroImage. 2018.
129. Liu Z, Kee Y, Zhou D, Wang Y, Spincemaille P. Preconditioned total field inversion (TFI) method for quantitative susceptibility mapping. Magnetic resonance in medicine. 2017;78(1):303-15.
130. Sun H, Seres P, Wilman A. Structural and functional quantitative susceptibility mapping from standard fMRI studies. NMR in Biomedicine. 2017;30(4):e3619.
131. Schweser F, Deistung A, Sommer K, Reichenbach JR. Toward online reconstruction of quantitative susceptibility maps: superfast dipole inversion. Magnetic resonance in medicine. 2013;69(6):1581-93.
132. Meineke J, Wenzel F, de Marco M, Venneri A, Blackburn DJ, Teh K, et al. Motion artifacts in standard clinical setting obscure disease-specific differences in quantitative susceptibility mapping. Physics in medicine biology. 2018.